



Exploration of tropical landscape structures by an unmanned aerial vehicle in Sumatra

To gain the Master of Science degree (M.Sc.) in Tropical and International Forestry (TIF)
at the Faculty of Forest Sciences and Forest Ecology, Georg-August-University Göttingen

Presented by
Robin Victor Naumann
Born in Wiesbaden, Germany

Supervisors

1. Prof. Dr. Dirk Hölscher
2. Prof. Dr. Holger Kreft

Göttingen, 29th April 2015

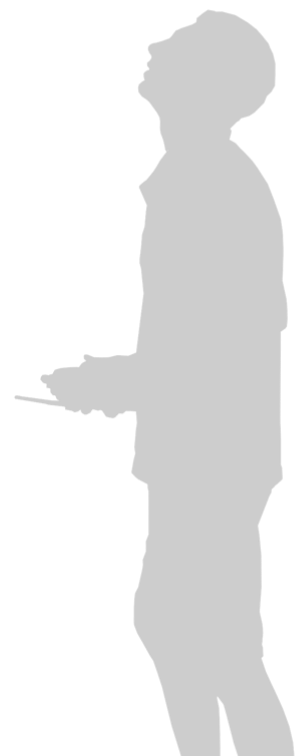


Table of contents

LIST OF TABLES	3
LIST OF FIGURES	4
ABBREVIATIONS	6
ABSTRACT	7
ZUSAMMENFASSUNG	8
INTRODUCTION	9
STUDY SITE	10
AIM OF THE STUDY	10
METHODS	12
MISSION PREPARATION	12
<i>Unmanned Aerial Vehicle (UAV)</i>	12
<i>Digital Camera</i>	14
<i>Near-infrared</i>	15
<i>Canon Hack Development Kit</i>	17
MISSION PLANNING	18
<i>Mission Planning for the Study Area</i>	20
MISSION IMPLEMENTATION	22
<i>Location</i>	22
<i>Ground control</i>	23
<i>UAV Assembly</i>	24
<i>Preflight Check</i>	25
<i>Takeoff</i>	26
<i>Landing</i>	27
DATA PROCESSING	28
<i>Editing GPS Information of Images</i>	28
<i>Digital Surface Model and Orthorectified Photomosaic</i>	30
<i>Calculating the Correlation of Altitudes</i>	32
<i>Calculating the Normalized Difference Vegetation Index</i>	32
<i>Comparison of DSM and NDVI</i>	33
<i>Thematic Map</i>	34

RESULTS	35
ORTHORECTIFIED PHOTOMOSAIC.....	36
DIGITAL SURFACE MODEL	37
CORRELATION OF ALTITUDES	38
NORMALIZED DIFFERENCE VEGETATION INDEX.....	39
COMPARISON OF DSM AND NDVI	41
THEMATIC MAP AND AREA DISTRIBUTION.....	42
DISCUSSION	44
EVALUATION OF METHODS	44
ORTHORECTIFIED PHOTOMOSAIC.....	46
DIGITAL SURFACE MODEL	48
CORRELATION OF ALTITUDES	49
NORMALIZED DIFFERENCE VEGETATION INDEX.....	49
THEMATIC MAP	51
CONCLUSION	52
REFERENCES	53
APPENDIX.....	56
ACKNOWLEDGEMENTS	60
STATUTORY DECLARATION	61

List of tables

- TABLE 1.** CALCULATED SPECIFICATIONS OF THE ORTHOMOSAIC 36
- TABLE 2.** CALCULATED SPECIFICATIONS OF THE DSM 37
- TABLE 3.** DISTRIBUTION AND SIZE OF AREAS WITHIN THE RESEARCH AREA ACCORDING TO THE PIE CHART 42
- TABLE 4.** DISTRIBUTION AND SIZE OF AREAS WITHIN THE RESEARCH AREA ACCORDING TO THE THEMATIC MAP 43
- TABLE 5.** SPECIFICATION OF THE CANON POWERSHOT SX260 HS DIGITAL CAMERA (CANON, 2014) 56
- TABLE 6.** SPECIFICATIONS OF THE UAV (3DR, 2014) 56
- TABLE 7.** POSITION AND ID OF INDIVIDUAL TREES 57
- TABLE 8.** EXCLUDED ALTITUDES FROM CERTAIN EXPERIMENTAL TREE ISLAND, DUE TO INCORRECT GPS MEASUREMENTS..... 59

List of figures

FIGURE 1. SKYWALKER UAV	12
FIGURE 2. 1) MOTOR AND PROPELLER; 2) PIXHAWK AUTOPILOT; 3) LIPO BATTERY.....	13
FIGURE 3. 1) CAMERA EMBEDDED ON SPONGE; 2) MOUNTING THE CAMERA INTO THE FUSELAGE; 3) CAMERA HOLE AT UAV BOTTOM	14
FIGURE 4. SCHEMATIC WAVELENGTH TRANSMISSION OF ROSCO #2007 FILTER	15
FIGURE 5. SPECTRAL REFLECTANCE CURVE FOR HEALTHY GREEN VEGETATION	16
FIGURE 6. SOFTWARE INTERFACE OF 'MISSION PLANNER', DISPLAYING WAYPOINTS AND FLIGHT PATH OF A MISSION	18
FIGURE 7. SCHEMATIC ILLUSTRATION OF SIDE OVERLAP AND FRONT OVERLAP.....	19
FIGURE 8. FLIGHT PATHS OF MISSIONS	20
FIGURE 9. A SCHEMATIC REPRESENTATION OF TWO DIFFERENT MISSIONS.....	21
FIGURE 10. MISSION PLANNER INTERFACE SHOWING 'HOME LOCATION' (YELLOW).....	22
FIGURE 11. GROUND CONTROL STATION	23
FIGURE 12. 1) ASSEMBLING UAV; 2) PREPARING CAMERA	24
FIGURE 13. DETERMINATION OF THE CENTER OF GRAVITY WITH HORIZONTAL ALIGNMENT.....	24
FIGURE 14. LAUNCHING THE UAV FOR TAKEOFF.....	26
FIGURE 15. SCHEMATIC ILLUSTRATION OF THE LANDING PROCESS.....	27
FIGURE 16. DEFINING THE TIME SHIFT OF PICTURES AND GPS TRACK	29
FIGURE 17. SCHEMATIC ILLUSTRATION OF STEREOSCOPIC TRIANGULATION	30
FIGURE 18. APPLIED COLOR SCHEME 'NRWC' IN QGIS	31
FIGURE 19. SCHEMATIC EXAMPLE OF COMPARISON OF DSM WITH NDVI VALUES.....	33
FIGURE 20. ORTHORECTIFIED PHOTOMOSAIC OF THE RESEARCH AREA	36
FIGURE 21. DIGITAL SURFACE MODEL OF THE RESEARCH AREA	37
FIGURE 22. CORRELATION OF ALTITUDES, INCLUDING ALL MEASUREMENTS	38
FIGURE 23. CORRELATION OF ALTITUDES, EXCLUDING INCORRECT MEASUREMENTS.....	38
FIGURE 24. ORTHORECTIFIED PHOTOMOSAIC OF THE RESEARCH AREA, WITH NIR, GREEN AND BLUE COLOR CHANNELS.....	39
FIGURE 25. ILLUSTRATION OF THE MISSING NORTHERN PART	39
FIGURE 26. FIVE CLASSES OF THE NDVI COLOR MAP.....	39
FIGURE 27. COLOR MAP OF CALCULATED NDVI.....	40
FIGURE 28. SCHEMATIC DESCRIPTION OF THE COMPARISON	41
FIGURE 29. GREY SCALE DSM OVERLAID WITH THE HIGHEST REFLECTANCE VALUES OF THE NDVI	41
FIGURE 30. PIE CHART OF THE AREA DISTRIBUTION WITHIN THE RESEARCH AREA	42
FIGURE 31. THEMATIC MAP OF THE RESEARCH AREA	43
FIGURE 32. LEGEND OF THE THEMATIC MAP.....	43
FIGURE 33. SCHEMATIC ILLUSTRATION OF THE 'FAÇADE PROBLEM', DUE TO INSUFFICIENT OVERLAP	45
FIGURE 34. ORTHORECTIFIED PHOTOMOSAIC OF THE RESEARCH AREA (2014)	47
FIGURE 35. SATELLITE IMAGE OF THE RESEARCH AREA	47
FIGURE 36. DISPLAY OF THE KEYPOINT MATCHES	58

FIGURE 37. REPRESENTATION OF THE NUMBER OF OVERLAPPING IMAGES COMPUTED FOR EACH PIXEL OF THE ORTHOMOSAIC..... 58

FIGURE 38. THE OFFSET BETWEEN THE INITIAL AND COMPUTED IMAGE POSITIONS 58

Abbreviations

CHDK	Canon Hack Development Kit
CMOS	Complementary Metal-Oxide-Semiconductor
COG	Center of Gravity
CRC	Collaborative Research Centre 990
DSM	Digital Surface Model
EFForTS	Ecological and socio-economic functions of tropical lowland rainforest transformation systems
GPS	Global Positioning System
IPB	Bogor Agricultural University
LED	Light-emitting Diode
Li-ion	Lithium-ion Battery
LIPI	Indonesian Institute of Science
LiPo	Lithium Polymer Battery
NDVI	Normalized Difference Vegetation Index
NIR	Near-Infrared
SFB	Sonderforschungsbereich
STICK	Simple Tool for Installing CHDK
UAV	Unmanned aerial vehicle
UNJA	University of Jambi
UNTAD	Tadulako University
VIS	Visible
GSD	Ground Sampling Distance

Abstract

Unmanned aerial vehicles (UAV) are constantly gaining approval and usage for a wide range of natural resource management and ecology. An UAV enables cost-effective autonomous aerial image acquisition and bridges the gap between ground observations and imagery taken from conventional manned aircrafts or satellites. It is the aim of this thesis to contribute to a greater understanding and to test the performance efficiency of UAVs in the specific field of tropical forest ecology. I conducted this study as part of the Collaborative Research Centre (CRC) 990, in the lowlands of Jambi province in Sumatra, Indonesia. I used a fixed-wing UAV that was either equipped with a default compact system camera or a modified compact system camera, capable to record respectively photographs in visible or near-infrared light. Photogrammetric image processing enabled the generation of an orthorectified 2D photomosaic and a 3D digital surface model (DSM) with a sub-decimeter level resolution for an area of 628 ha. Furthermore, I used the near-infrared pictures to calculate the 'normalized difference vegetation index' (NDVI) and produced a thematic map of the research area. The results emphasize that an UAV can be an appropriate and reliable tool in the field of tropical forest ecology. With continuous technological progress, increasingly affordable prices and an adapted legislation, UAVs will become more popular and continue to play an important role in the future.

Zusammenfassung

In Bereichen des Ressourcenmanagements und der Ökologie wird der Einsatz von unbemannten Luftfahrzeugen (Englisch: Unmanned aerial vehicles, UAV) immer beliebter. Sie ermöglichen die kostengünstige Gewinnung von Luftbildaufnahmen. Dabei reihen sich unbemannte Luftfahrzeuge zwischen Untersuchungen am Boden und Luftaufnahmen aus bemannten Flugzeugen oder Satelliten ein. Ziel dieser Arbeit ist es, zu einem besseren Verständnis beizutragen und die Leistungseffizienz von UAVs im Bereich der Tropenwaldökologie zu testen. Die Studie wurde im Rahmen des Sonderforschungsbereichs (SFB) 990 realisiert, in der Provinz Jambi auf Sumatra in Indonesien. Um Luftbilder zu erfassen, verwendete ich ein unbemanntes Tragflächenflugzeug, in welchem ich entweder eine normale Digitalkamera oder eine modifizierte Digitalkamera montierte. Diese Digitalkameras ermöglichten Aufnahmen im sichtbaren oder nahinfraroten Bereich des Lichts. Durch photogrammetrische Bildverarbeitung wurden für eine Fläche von 628 ha ein Orthophotomosaik und ein digitales Oberflächenmodell erstellt. Darüber hinaus wurden die Nahinfrarot-Bilder verwendet, um den normalisierten differenzierten Vegetationsindex (NDVI) zu berechnen und eine thematische Karte der Region zu erstellen. Die Ergebnisse unterstreichen, dass ein unbemanntes Luftfahrzeug ein geeignetes und zuverlässiges Werkzeug auf dem Gebiet der Tropenwaldökologie sein kann. Durch kontinuierlichen technologischen Fortschritt, erschwinglichere Preise und eine angepassten Gesetzgebung werden unbemannte Luftfahrzeuge zukünftig eine wichtige Rolle spielen.

Introduction

Unmanned aerial vehicles (UAV) for aerial data collection purposes are constantly gaining approval and usage for a wide range of natural resource management applications and in the field of ecology (Watts, Ambrosia and Hinkley 2012).

So far, most researchers and experts had to rely on imagery from satellites and conventional manned aircrafts, for mapping and monitoring purposes. However, this kind of data acquisition might not be always possible, especially due to financial constraints. Furthermore, the frequent occurrence of clouds in the humid tropics makes it difficult to obtain clear and up to date aerial pictures from remote sensing satellites and aircraft sensors, as these areas are often obscured (Koh and Wich 2012). The implementation of ground surveys is another frequently used type of regional data acquisition. This alternative however, can be time-consuming, labor intensive and expensive, particularly in remote areas (Koh and Wich 2012).

The application of UAVs bridges the gap between imagery taken from conventional manned aircrafts or satellites and ground observations (d'Oleire-Oltmanns, et al. 2012). Although the military has used UAVs for decades, fully autonomous UAVs have recently become commercially available at reasonable cost for civil applications (Watts, Ambrosia and Hinkley 2012). Additionally, they are light in weight and very easy to deploy and retrieve (Küng, et al. 2011).

For this reason, the utilization of UAVs represents a cost-effective aerial image acquisition with optimal spatial and temporal resolutions for the respective research question or application (d'Oleire-Oltmanns, et al. 2012).

The use of low-cost UAVs in scientific research is a relatively new approach and there is no uniform standard procedure. Users without long-standing involvement in this field may face a steep learning curve, which can be a barrier to entry (Watts, Ambrosia and Hinkley 2012).

Study site

The study was carried out within the framework of the Collaborative Research Centre (CRC) 990 named “Ecological and socio-economic functions of tropical lowland rainforest transformation systems” (EFForTS). The aim of the CRC 990 is to examine the reasons and effects of the transformation of tropical lowland rainforest into agricultural landscapes in Sumatra, Indonesia and to provide information on how to combine both agricultural land-use and conservation strategies (CRC 990 2012). The CRC 990 is a long-term collaboration between the University of Göttingen, the University of Jambi (UNJA), Bogor Agricultural University (IPB), Tadulako University (UNTAD) and the Indonesian Institute of Science (LIPI) (CRC 990 2012).

The CRC 990 project is divided into several subprojects and this study is part of the subproject B11 with the title: ‘Biodiversity enrichment in oil palm plantations: ecological and socio-economic impacts’ (referred to as ‘B11’ hereafter; www.uni-goettingen.de/crc990). The subproject B11 is an enrichment planting experiment within a large-scale oil palm plantation in the lowlands of Jambi province (Sumatra, Indonesia). Many tropical landscapes are undergoing rapid transformations. In case of the establishment of oil palm plantations on former rainforest land, this is associated with a strong decline in animal and plant diversity. In order to restore biodiversity and to study successional dynamics in an already largely depleted oil palm landscape, 52 experimental tree islands of varying size, tree species composition and diversity were established within an oil palm plantation. As part of the B11 project, the fieldwork for this thesis was realized at its study site between 8th August and 14th August 2014.

Aim of the study

It is the aim of this thesis to contribute to a greater understanding and to test the performance efficiency of UAVs in the specific field of tropical forest ecology. The potential advantages of an unmanned platform depend on many factors, such as aircraft, sensor types and mission objectives (Watts, et al., 2012). Two main types of available UAVs are suitable for surveying purposes, either a fixed-wing model or a multicopter system.

The fixed-wing UAVs need air movement under their wings to generate lift and therefore, they have to stay constantly in forward motion. Unlike the fixed-wing models, the multicopters are able to fly in every direction, horizontally and vertically, as well as hover in a fixed position (APM 2014). However, this technique consumes much more energy compared to a fixed-wing UAV. Fixed-wing UAVs have good gliding properties and are usually operated only by one

motor (APM 2014). Consequently, they are more energy-efficient and have a longer flight duration (about 30 to 40 minutes) than most multicopters (about 5 to 15 minutes) (APM 2014). In addition, the wings have a great lifting surface and therefore, more payload can be carried onboard of a fixed-wing UAV (Watts, Ambrosia and Hinkley 2012). To be able to fly over the entire experimental area of the B11 project and its periphery (about 600 ha), I used a fixed-wing UAV, equipped either with a default compact system camera or a modified compact system camera, capable to record aerial photographs respectively in visible (VIS) and near-infrared (near-infrared) light (Public Lab 2013). Photogrammetric image processing enabled the generation of an orthorectified 2D photomosaic and a 3D digital surface model (DSM) with a sub-decimeter level resolution. Furthermore, I used the near-infrared pictures to calculate the ‘normalized difference vegetation index’ (NDVI) and produced a thematic map of the region, based on the generated orthomosaic.

Methods

Mission Preparation

Unmanned Aerial Vehicle (UAV)

For the development of a map resulting from aerial photography of the Humus Indo research area, I used a Skywalker airframe as UAV platform (*Figure 1*), a fixed-wing aircraft with a wingspan of 188 cm and a length of 129 cm (3DR 2014). This aircraft model is composed of five individual parts: the fuselage, two wings with ailerons, a tail boom with vertical stabilizer and the rudder attached to it, as well as the horizontal stabilizer with the elevator. Apart from the tail, the other four individual components consist of lightweight expanded polyolefin foam. The tail is made of fiberglass-reinforced plastic. Before a flight, the aircraft requires basic assemblage of these components. The setup enables a lightweight (3 kg, incl. battery) and a robust fixed-wing platform construction with an internal volume of 280 cm³. The design allows carrying an extra equipment payload of 2 kg (3DR 2014).



Figure 1. Skywalker UAV

The UAV is driven by an electrical propulsion system (RC Tiger Motor 2820, 830 kv) and an 11 x 7 inches propeller (*Figure 2*). Four small electrical servomotors are responsible for the movement of the ailerons, the rudder and the elevator. The navigation of the aircraft, the individual servos and the flying speed, can be remotely controlled through radio signals from a hand-held radio transmitter or in the case of autonomous flights, by an autopilot system (3DR 2014).

I installed the Pixhawk flight controller (*Figure 2*), designed by the PX4 open-hardware project and manufactured by 3D Robotics as autopilot system in the Skywalker airframe, which is optimized to provide control and automation for flight navigation software (APM 2014). It is additionally connected to a digital airspeed sensor and a magnetometer compass module. These sensors are required to control the flight characteristics and to determine the flight direction and altitude (APM 2014). To make the handling of the UAV safer and easier, a safety switch button for arming and disarming the engine, a buzzer and an external multi-color LED (light-emitting diode) indicator are additionally connected on the outer casing (3DR 2014). The UAV system furthermore supplies a 433 MHz frequency telemetry radio set, providing an air-to-ground data link between the autopilot and a ground station computer (3DR 2014). Radio telemetry allows the ground station computer to communicate with the UAV wirelessly for viewing in-flight data (e.g.: GPS (Global Positioning System) coordinates, position on a map, battery voltage, heading, waypoint navigation, distances, flying speed, artificial horizon) and for changing missions spontaneously. The range of this telemetry antenna averages between 300 m and 500 m (APM 2014).

All electrical devices were powered by a 4S 6000 mA×h 35C lithium polymer battery (LiPo) mounted in the interior of the fuselage (*Figure 2*). On average, this gives the UAV a maximum flight duration of 35 to 40 minutes, depending on the weather conditions (3DR 2014). I secured the battery by a hook and loop fastener for quick installment and removal, while I firmly attached the other mentioned components into the fuselage.



Figure 2. 1) Motor and propeller; 2) Pixhawk autopilot; 3) LiPo battery

(3drobotics.com)

Digital Camera

To capture aerial pictures of a territory of interest, I installed a camera on board of the UAV. For the photographic images, I mounted either a customary or a modified version of the Canon PowerShot SX260 HS camera into the fuselage (*Figure 3*). A CMOS (complementary metal-oxide-semiconductor) image sensor (6.17 mm x 4.55 mm) with a resolution of 12.1 megapixels (4000 x 3000 pixels) is responsible for the picture generation in JPEG format (Canon 2014). The two cameras are provided with internal GPS to add geographical identification metadata (latitude and longitude coordinates) to the photographs. The lithium-ion battery (Li-ion) manages approximately 600 shots, before it has to be recharged. The Canon PowerShot SX260 HS cameras are each equipped with a 16 gigabyte SD memory card and weigh 231 g (Canon 2014).

Due to the generous internal space of the Skywalker model, there is enough room to store the compact system camera and battery. The camera position in the fuselage is directly under the wings, perpendicular to the center of gravity (COG), so that the influences of flight movements are as low as possible on the taken pictures to avoid blurring (3DR 2015). During flight, the electric motor of the UAV produces vibrations, which can also result in blurred photographs. For this reason, I additionally embedded the camera on a common kitchen sponge (*Figure 3*), when installing it in the fuselage. This stable placement can avoid vibration blur to a certain degree. I mounted the camera lengthwise into the fuselage, parallel to the flying direction. To achieve aerial pictures perpendicular to the ground, I mounted the camera with the lens downwards and the pictures were captured through a hole at the UAV bottom (\varnothing 6 cm) (*Figure 3*).



Figure 3. 1) Camera embedded on sponge; 2) Mounting the camera into the fuselage; 3) Camera hole at UAV bottom

Near-infrared

In addition to visible light photographs, I also took aerial imagery in the near-infrared spectral range, to calculate the normalized difference vegetation index (NDVI) of the area. Rouse et al. (1973) from the Remote Sensing Centre of Texas A&M University first implemented the NDVI.

For this purpose, I modified one Canon PowerShot SX260 HS camera by replacing the filter in front of the sensor. The incorporated CMOS image sensor of the camera is capable to capture near-infrared wavelength, but is restricted by an integrated infrared block filter to the wavelength of red, green and blue, to mimic the spectral color sensitivity of the human eye (Taylor, 2013). For modification, I removed the original internal near-infrared high-pass filter in front of the CMOS sensor and replaced it with a specific Rosco #2007 band-pass filter (Taylor 2013). This modification is permanent and requires adequate care to protect the sensitive internal components. Scratches, fingerprints or dust particles on the image sensor can significantly affect the quality of the pictures (Taylor 2013). Therefore, I wore anti-static gloves during the modification of the camera. The blue filter is blocking red light, but extends the incidence of light into near-infrared (*Figure 4*).

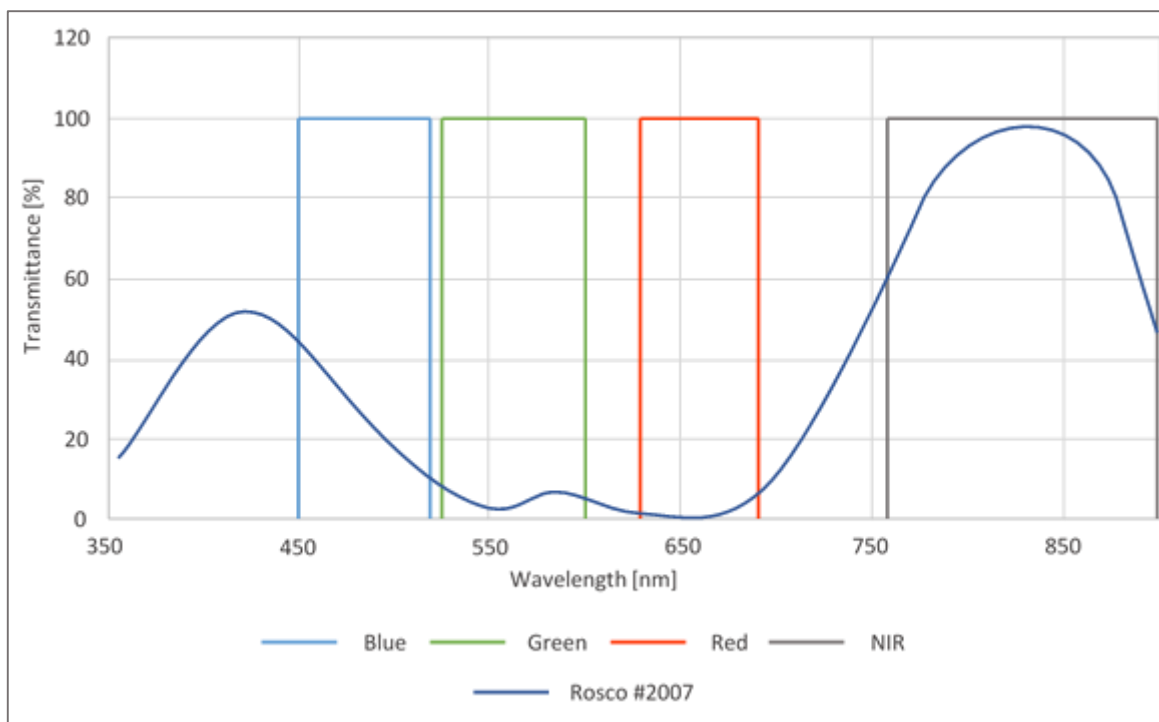


Figure 4. Schematic wavelength transmission of Rosco #2007 filter. (Adapted from: publiclab.org)

The strong blue color that reaches the camera's sensor, due to the new Rosco #2007 filter, overpowers the standard white balance settings of the Canon PowerShot SX260 HS camera (Public Lab 2013). To compensate this, I had to adjust the white balance manually. As reference for the new “white”-value, I used a sheet of blue origami paper, so that the camera keeps blue for white. When custom white balance is implemented properly, infrablue photos of healthy plants appear orange yellow (Public Lab 2013).

Vegetation absorbs blue and red light for energy production through photosynthesis, but it reflects light in the green and particular in near-infrared spectral range (*Figure 5*). In the near-infrared part of the spectrum, reflectance of living vegetation increases strongly, leading to reflection fractions of 40 – 50 % in the wavelength range from 0.7 to 1.3 μm . The typical reflection pattern of plants facilitates the differentiation of vegetation and non-vegetation on pictures. In cases of stress or disease, the chlorophyll content of a plant decreases and the reflection of near-infrared energy is reduced. Therefore, variations in the reflection can indicate the health status of a plant (Jones and Vaughan 2010).

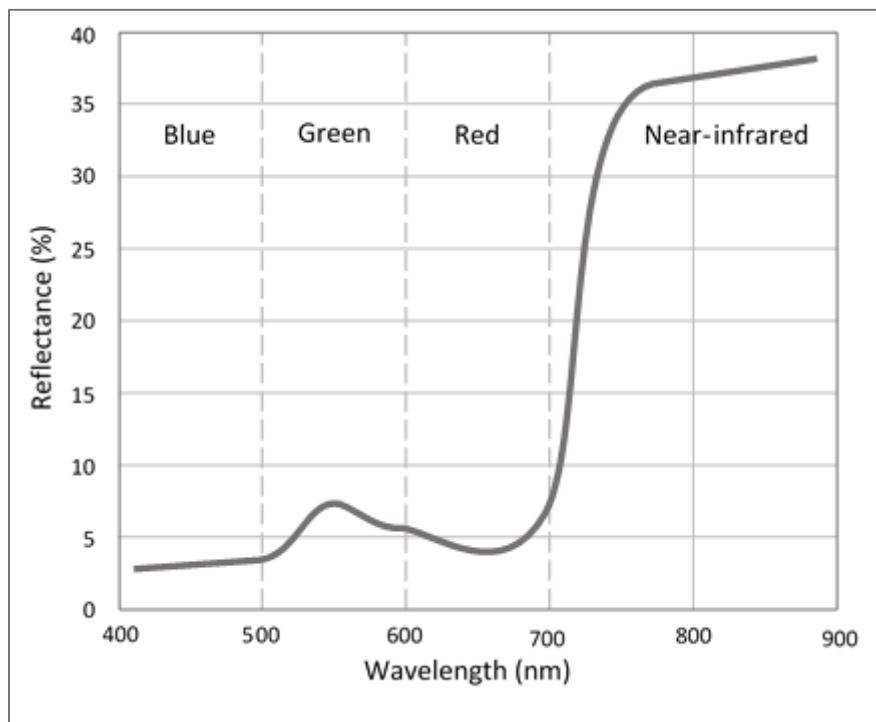


Figure 5. Spectral reflectance curve for healthy green vegetation (Adapted from: www.sciencereay.com)

Canon Hack Development Kit

I modified the original firmware of the Canon cameras with the canon hack development kit (CHDK). The CHDK loads from an SD memory card into the RAM memory of the camera and provides supplementary functionalities in addition to the pre-installed camera firmware (CHDK 2014). I conducted the software upload with the "Bootable SD Card" method, which required setting up an SD card especially for this purpose. I used a utility called "Simple Tool for Installing CHDK" (STICK). The STICK is a Java application that downloads the appropriate parameters, formats an SD card for making it bootable and copies the appropriate files onto the card (Mitchell 2013). It is not a permanent intervention and only enhances the capabilities of the camera. The CHDK enables the implementation of a customized intervalometer script to trigger photographs at predefined time intervals (e.g. every three seconds). Furthermore, the script allows defining several other parameters, including a time delay before the camera starts taking pictures and an automatic shutdown.

Mission Planning

The UAV can be steered manually, semi-autonomous or fully autonomous. For the acquisition of large aerial imagery, the automatic flight option is preferred. Depending on the spatial circumstances, manual or semi-autonomous takeoff or landing is occasionally necessary. In fully automated flight missions or after reaching the desired flight altitude, the autopilot system takes over to control the UAV. If the flight is controlled by the autopilot, the paths of a mission have to be planned and programmed with a corresponding software and uploaded to the autopilot system. For this purpose, I used the Mission Planner (version: 1.3.16), created by Michael Osborne (APM 2014).

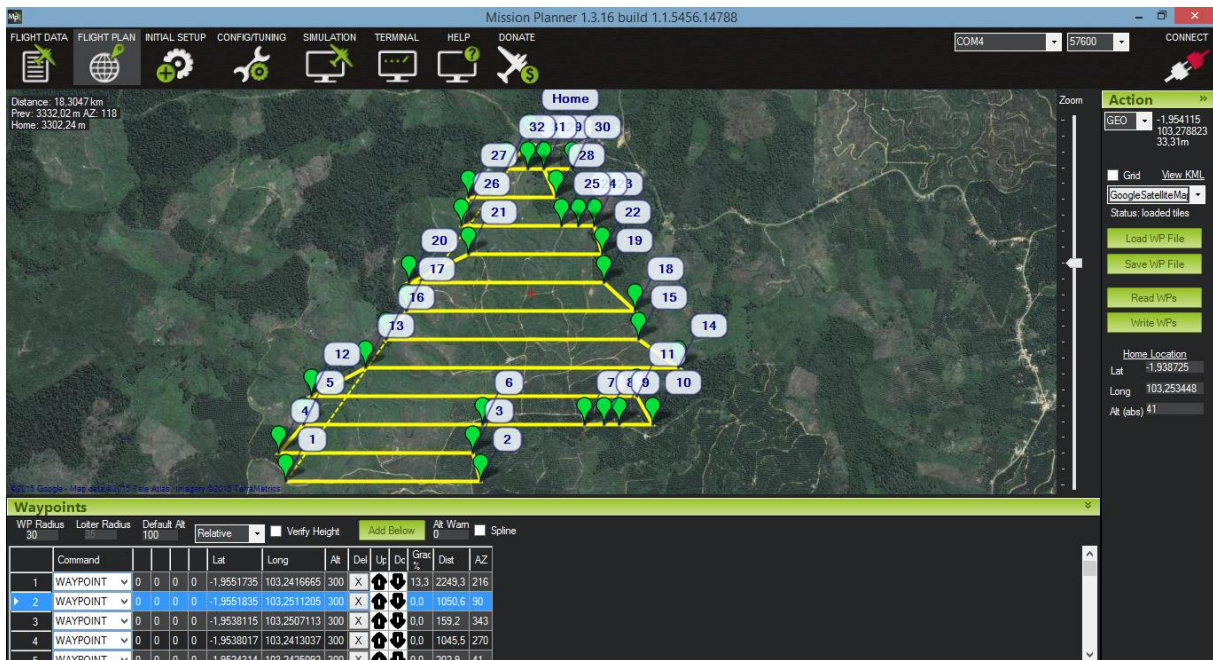


Figure 6. Software interface of 'Mission Planner', displaying waypoints and flight path of a mission.

To plan a mission, it is necessary to have some preliminary information about the area of interest in order to know the spatial circumstances. I used the boundary coordinates of the B11 subproject to load a shapefile-based polygon of the area into the map interface (e.g. Google Satellite Map) of the Mission Planner. Individual waypoints can be created at the targeted location by a point-and-click setup on the flight plan canvas (Figure 6). These waypoints define the intended course of the UAV. Each waypoint has its own assigned coordinates (longitude/latitude) and height. To capture images for the map, the UAV has to fly a lawnmower-like pattern in strips across the survey site. For this purpose, I automatically generated waypoints by using the survey grid tool of the Mission Planner (Figure 6). However, it is important to assess the environmental conditions on site and to adjust the flight plan, if necessary.

Depending on the configuration, I had to consider and adapt the performance and spatial scope of a mission, the altitude, the track distance, the flying speed and the recurring capture of pictures, as they essentially influence the flight mission and results. The frontal overlap and side overlap are determining the number of recorded pictures and the distance between images, based on the projected ground area that each image will cover, called footprint (*Figure 7*). An increasing front overlap and side overlap improve the accuracy of the map, while increasing flight time. During the survey, the front overlap was time-based as I used a consistent interval time of three seconds, while the side overlap was set to 50 %, according to Drone Mapper (2012).

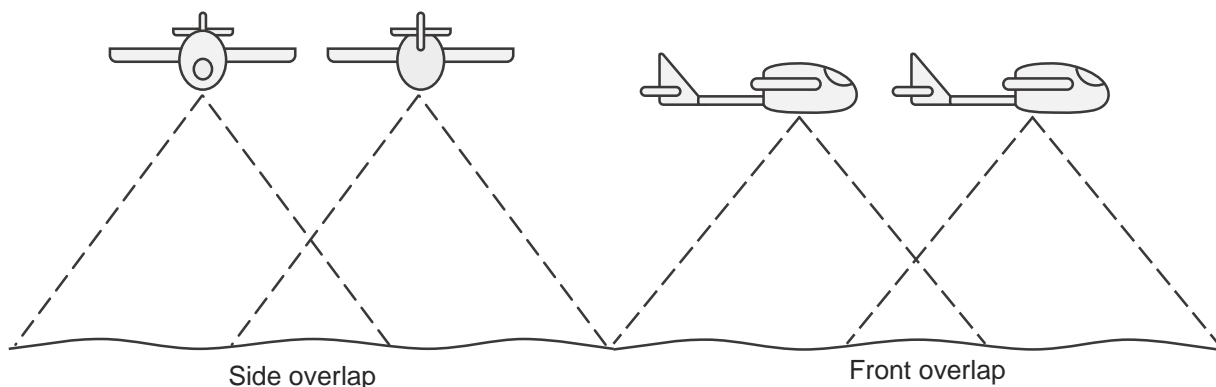


Figure 7. Schematic illustration of side overlap and front overlap

The altitude is determining the spatial resolution. The closer the UAV is flying to the earth's surface, the more details are captured on an image. However, an increased ground resolution also results in a smaller footprint of the area and this minimizes the distance between grid strips. Missions at a lower altitude have a higher spatial resolution, but a longer flight time, if the same area has to be covered. The degree of information in an aerial image is always depending on the outcome. Although a higher resolution results in a higher volume of data, it will not necessarily produce a higher content of information (e.g. counting of single fruits on a tree or mapping of land-use types).

Mission Planning for the Study Area

No recent spatial data with a high resolution were available for the research area of the subproject B11. The aim of this thesis was therefore, to produce a current aerial map of B11's research area and its periphery with a sufficient resolution, so that oil palms and other forms of vegetation can be distinguished within the environment. To achieve this, I flew the UAV at 300 m altitude in a grid-pattern. Additionally, I implemented a flight along the boundary of the experimental area at 300 m altitude to explore the surrounding landscape (*Figure 8*). Moreover, the flight duration of the UAV and its setup are limited to 35 to 40 minutes by the power of the battery.



Figure 8. Flight paths of missions

Consequently, the covered area varied significantly during a mission, depending on its altitude. The lower the altitude, the denser the transects within the mission should be (Figure 9). To cover as much of the area with one battery-charge as possible, I chose to set the side overlap to 50 %, so that I could accomplish the missions at an altitude of 300 in single flights. The success of the missions also depended on weather conditions. If it was too windy or rainy, I did not conduct flights. In total, I conducted 12 missions between 8th August and 14th August 2014.

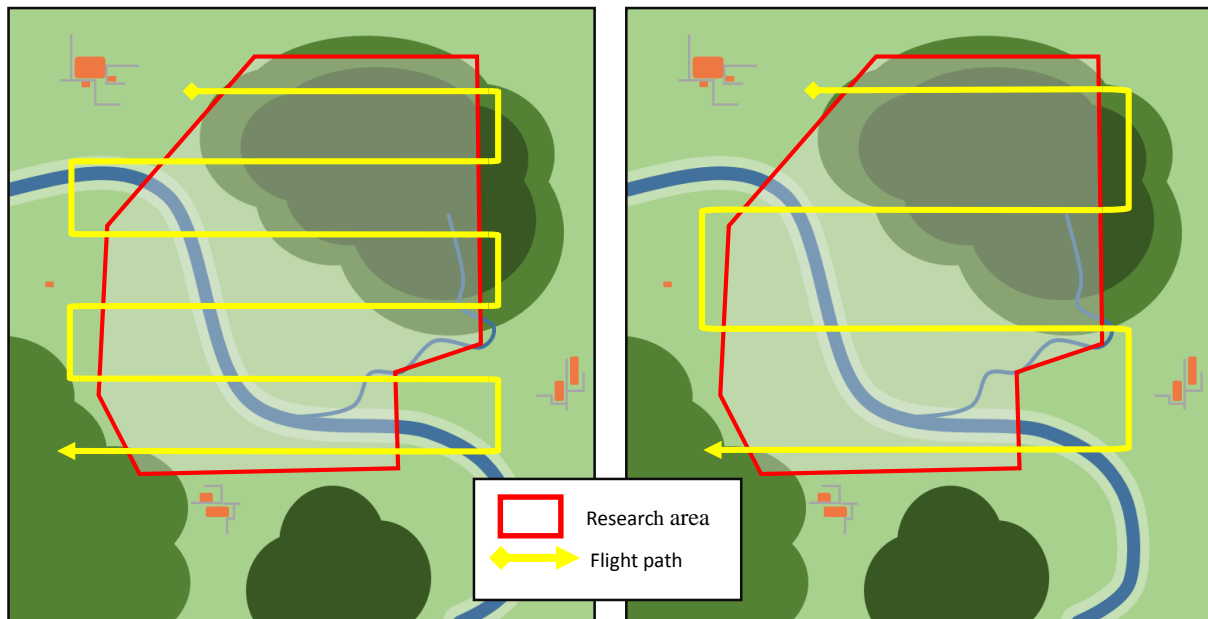


Figure 9. A schematic representation of two different missions. The mission on the left is accomplished at a lower altitude than the one on the right side and therefore, shows a longer track distance.

Mission Implementation

Location

I conducted the UAV missions above the area of Humus Indo in Jambi province in Sumatra, which is the research area of the B11 project of the CRC 990 (EFForTS). The vegetation of the study site is mainly comprised of oil palm monocultures (*Elaeis guineensis*). Only small patches of secondary vegetation occasionally occur.

During fieldwork, it was my first goal to search for a suitable takeoff and landing point ('home location') with an open space of at least 30 m in length. I chose to set the home location at S1°56'19.41" and E103°15'12.413" in the north of the research area, with a launching and approach corridor of approximately 60 m x 45 m (Figure 10).

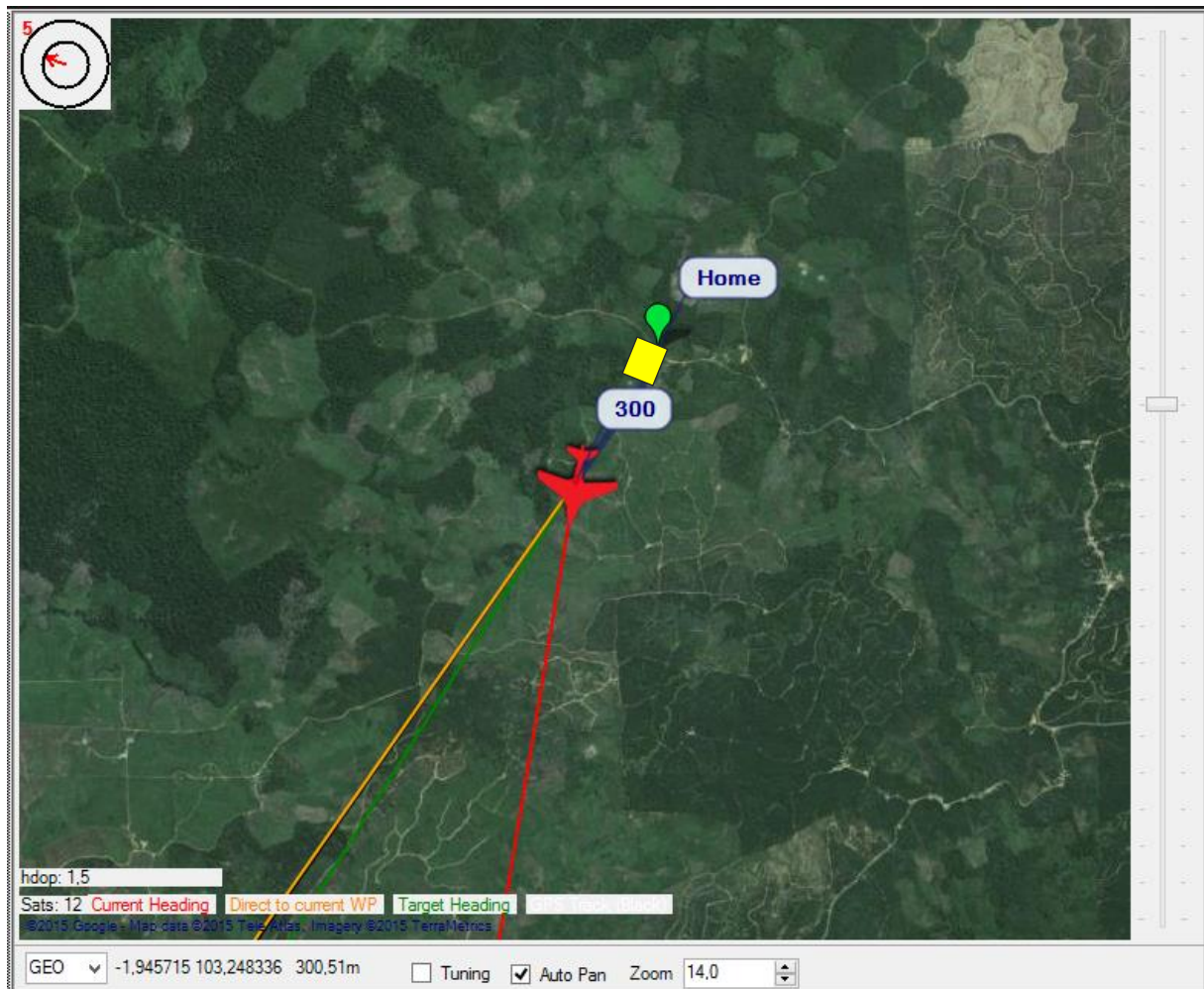


Figure 10. Mission Planner interface showing 'home location' (yellow)

Ground control

The first step was, to encamp the ground control station each morning at our home location. The referred ground control station consists of a computer with the Mission Planner software installed and a USB-connected 433 MHz frequency telemetry radio. To increase the range and to reduce interferences (APM 2014), I placed the telemetry antenna 1.80 m above the ground at the end of a pole (Figure 11).



Figure 11. Ground control station

UAV Assembly

Secondly, I mounted the UAV. I had to assemble all the individual parts (fuselage, wings, tail boom, vertical stabilizer and propeller) of the Skywalker aircraft. Next, I prepared the camera and the CHDK script according to the planned mission (*Figure 12*).



Figure 12. 1) Assembling UAV; 2) Preparing Camera

I implemented all missions with a camera trigger interval of three seconds. I adjusted the camera so that it only started to trigger after a delay of 60 seconds. In addition, the camera turned off when the mission was completed, to retract the lens and thus, to protect it while landing. I placed the camera, together with the fully charged battery, inside the fuselage. Both I secured with a hook, loop tape and fastener respectively. If the airplane is tail-heavy, the nose will rise. If the airplane is nose-heavy, the nose will fall. However, a horizontal alignment is sought (3DR 2015). For this reason, I balanced out the UAV by placing the index fingers to the center of gravity under the wings and by moving the battery slightly back or forth, until the aircraft was in a stable and level position (3DR 2015) (*Figure 13*).

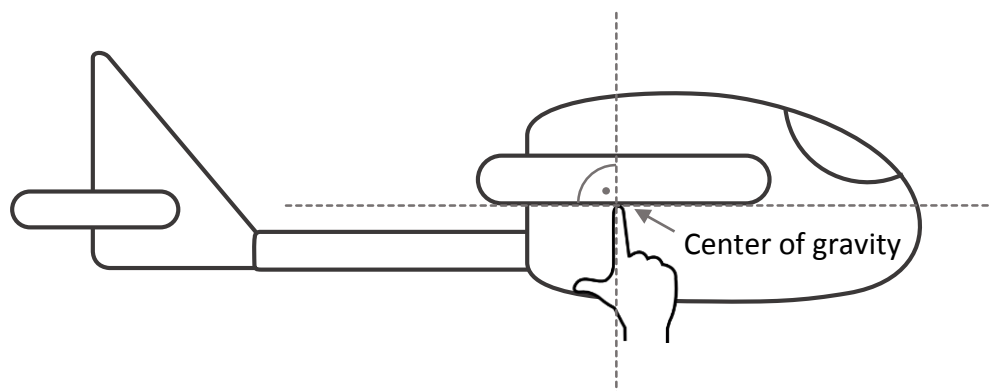


Figure 13. Determination of the center of gravity with horizontal alignment

Before I powered up the UAV, I always had to turn on the remote control first, for safety reasons. I had to ensure that the switches were set in “manual”-mode and the throttle stick was set fully down. Subsequently, I powered up the UAV and via telemetry radio, I established a connection between the UAV and the ground control computer. (3DR 2015)

When planning a mission, I had to consider the wind direction and speed. With winds of less than 6 m/s, I set the angle so that the UAV was flying into the wind. In winds from 7-10 m/s, I configured the flight path to travel perpendicular to the wind, so the UAV was flying in crosswind, as recommended by 3DR (3DR 2015). I uploaded the planned mission to the autopilot and afterwards downloaded the mission again to the computer to counter-check if the mission was uploaded correctly.

Preflight Check

To ensure a successful mission, it is advisable to undergo a preflight check, to make sure that all systems are functional and that the UAV was mounted correctly (3DR 2014). First, I checked if there is a stable GPS-connection (with at least six satellites) and that no obstacle (e.g. dust from a previous landing) blocked the airspeed sensor. Then I reviewed, if I assembled the wings, tail and tail boom correctly and if I secured the propeller tightly to the motor.

By performing controls in both manual and autopilot mode, I verified that the control surfaces respond to the control inputs and that the autopilot compensates for movements with counter-movements (e.g. when tilting the plain left, the left aileron tilts down and the right aileron tilts up or when tilting the plain up, the elevator tilts down). Furthermore, I raised the throttle slightly until the motor was spinning, to see if the propeller rotates in the right direction with a forward propulsion (3DR 2015).

Takeoff

Before takeoff, I switched on the camera and activated the CHDK script. I programmed the camera to start to trigger with a delay of 60 seconds. Before I conducted a takeoff, I needed to check the wind direction and speed on site at first. Moreover, I had to ensure that the takeoff flight path was clear of obstacles.

Two persons always carried out the takeoff. One person threw the UAV, while the other person was in charge of the controller. We always conducted the launching of the UAV against the wind, which ensured that the plane had the necessary air resistance to create a lift (*Figure 14*). Throwing the plane into the wind decreases the air resistance and can undermine the power it needs to take off (Main 2014). The autopilot automatically implemented the start and set up so that the UAV would climb in a pitch angle of 60 degree. After reaching an altitude of 50 m, the UAV began to head for the waypoints. Afterwards, the UAV was flying autonomously over the specified area, while the on-board camera captured aerial pictures every three seconds.



Figure 14. Launching the UAV for takeoff

Landing

After accomplishing a mission, the UAV returned to the starting point. The parameters were set so that the UAV was flying a circle pattern above the set home location with a diameter of 40 m and at an altitude of 100 m. Before landing, I checked that the lens of the camera had retracted.

Two persons were also required for landing operations, one for piloting the aircraft and another to serve as mission operator on the computer. To initiate the landing, the altitude was progressively reduced by creating a spirally motion through the application of commands at the ground control computer and by transmitting them by telemetry. This circular downward movement enables landing on a relatively small area, compared to a height reduction along a straight path (3DR 2015).

Once the UAV reached an altitude of 20 m, I manually took over the control. The UAV was flying into the wind on a 15 to 20 degree down-pitch angle. When the plane reached an altitude of 10 meters, the throttle was set down fully to turn off the motor and glide down. When the plane was one meter above the ground, the nose was pitched up (flare) to land on the body of the plane instead on the nose (3DR 2015). I accomplished all missions in the described way (Figure 15).

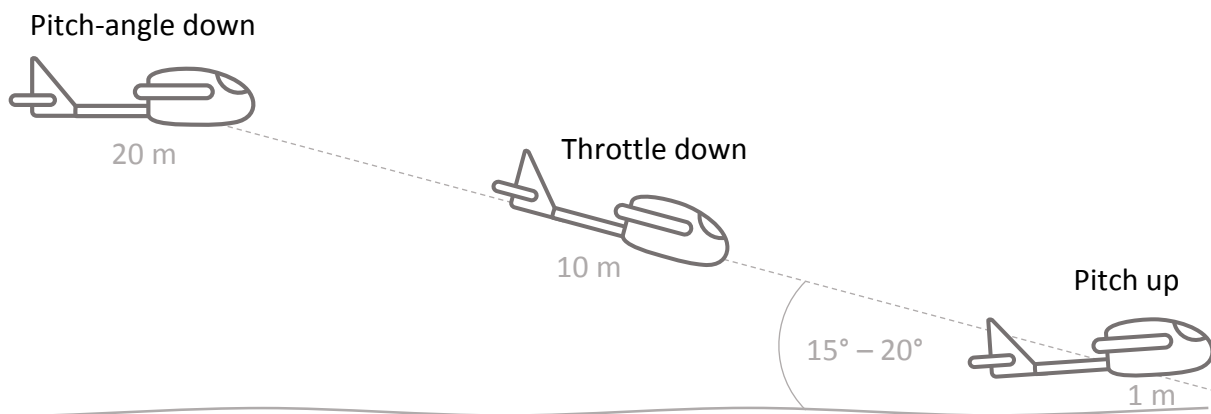


Figure 15. Schematic illustration of the landing process.

Data Processing

Editing GPS Information of Images

After a mission was completed, I downloaded the images from the SD card to a computer and an external hard disk drive. To produce a map, it is crucial that the individual pictures have corresponding geographical information in the metadata. Otherwise, the result would have no scale, orientation and absolute position information (Pix4D 2015). For each mission, the autopilot system recorded a respective log file, including information on geographical coordinates of the flight paths (3DR 2015). I used these GPS data, to georeference the captured images. Although the Canon PowerShot SX260 HS camera offers an internal GPS receiver, the position accuracy is inferior, due to a lower GPS refreshing rate compared to the autopilot system. (Pix4D 2015).

To adapt the picture's geographic information to the geographic information of the logged track, I compared their timestamps to detect whether there was a time shift among the metadata of the images and the track. For this, I used the freeware DNRGPS (Minnesota Department of Natural Resources 2015) to convert the track format from a "GPS Exchange Format" (.gpx) into an "Esri shapefile" (.shp). So it became possible to open the tracked flight path with a GIS-application like the open source software QGIS (QGIS 2015). In QGIS (version: Brighton 2.6.1), I could review and compare the time attributes of the individual track points with the timestamp of the related pictures (*Figure 16*). To view the picture's timestamp, I used the freeware IrfanView (Škiljan 2014).

I found a time shift of two seconds between the time stamps of the logged track and the captured pictures. To adjust the time shift in favor of the track, I adapted the time stamps in the metadata of the pictures by using the free software ExifToolGUI (Harvey 2012). After I matched the time, it was possible to provide the pictures with accurate GPS information. For this, I used the free software Geosetter (Schmidt 2011), which is geotagging pictures by using the GPS information of the recorded track.

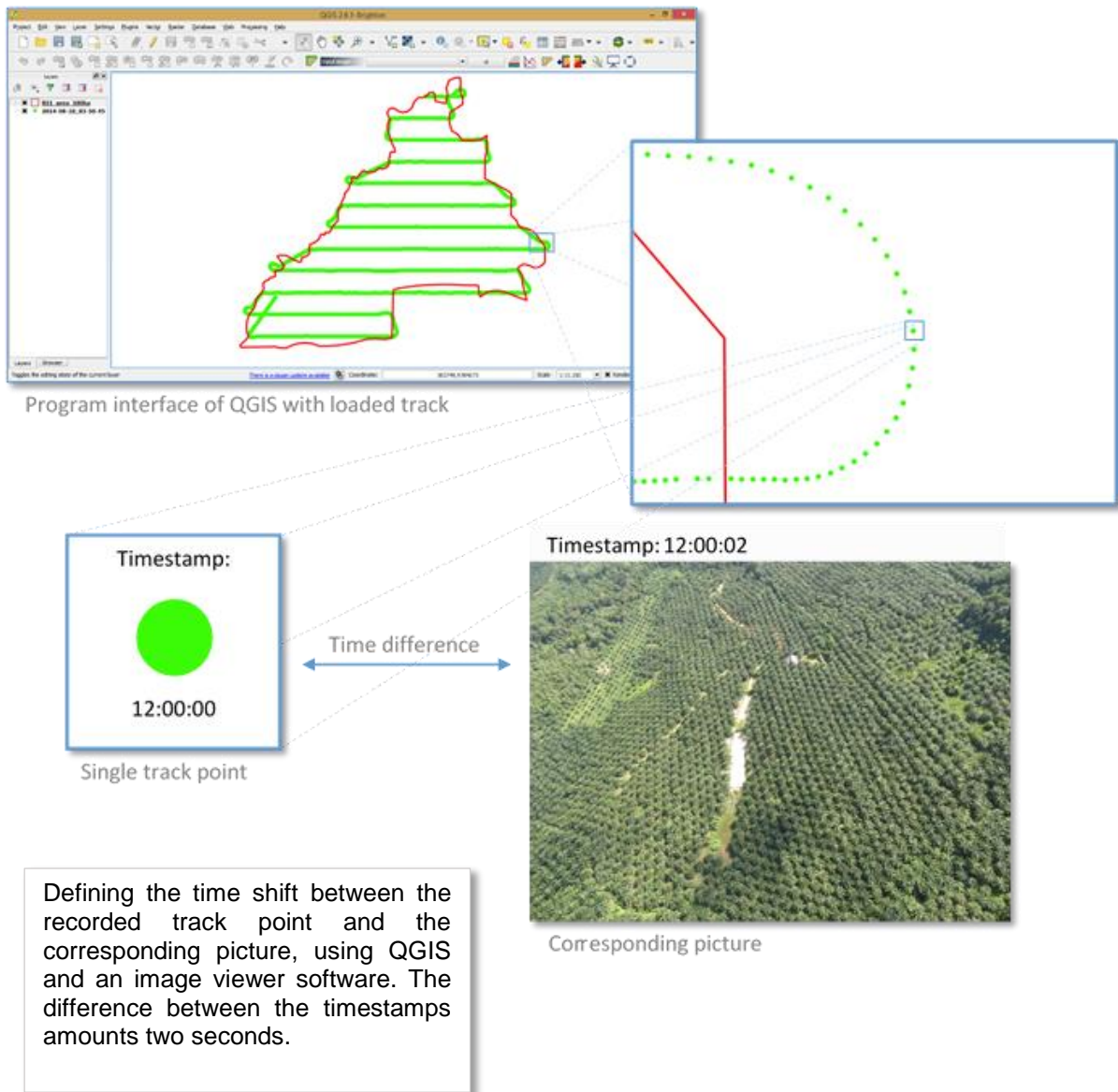


Figure 16. Defining the time shift of pictures and GPS track

Digital Surface Model and Orthorectified Photomosaic

Once the geographic information of the images were coinciding with those of the flight track, I was able to edit and compose them to one mosaic (O. Küng, Pix4D Webinar 1: Introduction to Modern Photogrammetry and Optimal Flight Plans 2014). I accomplished that through the application of aerial photogrammetry. By definition, photogrammetry is a measurement method in the field of remote sensing to determine the position and spatial extent of objects, based on photographic images. Measurements are not made directly at the objects, but indirectly at the images of the objects (Hanusch 2010).

To counteract the effect of nearby objects appearing larger than distant objects (and vice versa), specific relationships between two images showing the same object are taken into account. This is based on the stereoscopic triangulation of camera positions, distances and angles referring to an object on the ground (O. Küng, Pix4D Webinar 1: Introduction to Modern Photogrammetry and Optimal Flight Plans 2014) (*Figure 17*).

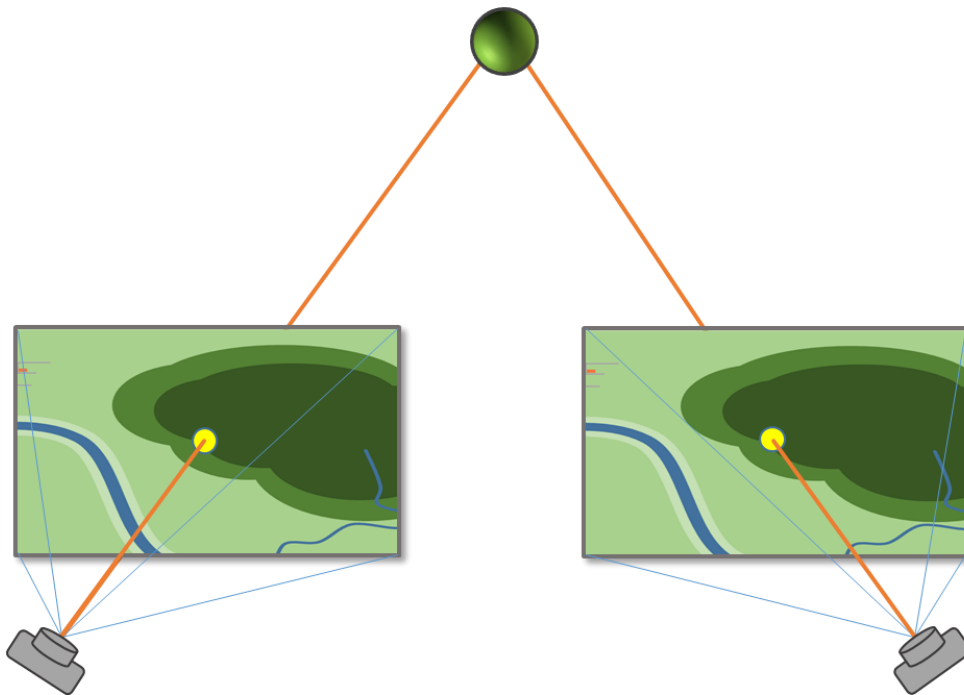


Figure 17. Schematic illustration of stereoscopic triangulation

To produce an orthomosaic of an area, which will occur as a 2-dimensional projection, it is necessary to have 3-dimensional information. Otherwise, the created mosaic will have distortions in distance measurements and position accuracy. Therefore, I arranged the aerial images according to the generated 3D model. This resulted in a DSM of the research area. In contrast to stitched pictures, orthomosaics are georeferenced and allow accurate measurements. This is the main difference between the result of simple image stitching and an orthorectified

2D photomosaic (O. Küng, Pix4D Webinar 1: Introduction to Modern Photogrammetry and Optimal Flight Plans 2014).

For image processing, I used the software Pix4Dmapper. This program is creating 3-dimensional information out of 2-dimensional pictures. After loading the correctly geotagged images, the software will check for keypoints (specific characteristics, e.g. corner of a building) in each picture. With an image resolution of 12 MP, about 60,000 keypoints are set per image. Subsequently, the software compared the keypoints from the different images to find matches between them. On average, the software found 6,000 matches per pair of images. From these keypoint matches, the program computed 3D points by triangulation. Thus, I was able to arrange the resulting 3D model, representing the surface elevation according to the GPS information. This geologically correct DSM serves as a scaffold, where the aerial images are projected on (O. Küng, Pix4D Webinar 1: Introduction to Modern Photogrammetry and Optimal Flight Plans 2014).

Using the aerial images taken by the UAV, the Pix4Dmapper software creates a DSM and an orthomosaic of the research area (O. Küng, Pix4D Webinar 1: Introduction to Modern Photogrammetry and Optimal Flight Plans 2014). I saved this generated DSM and orthomosaic in the image file format TIFF. In addition, I saved the orthomosaic as KML file, for displaying it in Google Earth and as HTML file, for displaying it in Google Maps with an internet browser.

Using the open source geographic information system QGIS (version: Brighton 2.6.1, www.qgis.org), the DSM has been graphically adjusted so that a visualization of the height differences was made clearer. First, a panchromatic image was created, displaying different heights in shades of gray. Bright gray levels and profundities by dark gray levels represent the elevations. Furthermore, I have created a color gradated DSM using the 'nrwc' scheme in QGIS (*Figure 18*).



Figure 18. Applied color scheme 'nrwc' in QGIS

Calculating the Correlation of Altitudes

For each of the 52 experimental tree islands, of project B11, GPS measurements were recorded on the ground. Not only were the positions recorded with a GPS unit, but also the respective altitudes. To determine how reliable the generated DSM is, I used the statistic open source software R (version: 3.1.2, www.r-project.org) to calculate the ‘Pearson’s correlation’ between the altitudes derived by GPS and the altitudes derived from UAV flights. A correlation between sets of data is a measure of how well they are related (Oestreich and Romberg 2014). ‘Pearson’s correlation’ can range from – 1 to 1. Thereby, a value of 1 indicates a perfect positive linear relationship, 0 indicates no linear relationship and a value of – 1 indicates a perfect negative linear relationship between data sets (Oestreich & Romberg, 2014).

Calculating the Normalized Difference Vegetation Index

The normalized difference vegetation index (NDVI) is described as a numerical indicator using visible and near-infrared bands of the electromagnetic spectrum. It is used to analyze remote sensing measurements and to assess, whether an observed target contains live green vegetation or not (Rouse, et al. 1973). Vegetation with a high vitality absorbs most of the visible light to produce energy. The chlorophyll in the leaves reflects a great portion of the near-infrared light. If the vegetation is sparse or not unhealthy, more visible light than near-infrared light is reflected, because the content of the chlorophyll inside the foliage is lower. The bigger the difference between the red light reflectance and the near-infrared light of an area, the higher is the chlorophyll content (Rouse, et al. 1973).

The NDVI algorithm subtracts the red reflectance values from the near-infrared and divides it by the sum of near-infrared and red bands (Rouse, et al. 1973).

$$NDVI = \frac{(NIR - R)}{(NIR + R)}$$

This formulation allows to handle the fact that two identical areas of vegetation could have different values, e.g. if one area is exposed to bright sunshine and another is shadowed from clouds. The bright pixels would all have larger values, and consequently a larger absolute difference between the bands. This is avoided by dividing by the sum of the reflectance (Rouse, et al. 1973).

I used the Pix4Dmapper software to compute the NDVI of the research area. For the NDVI calculation, near-infrared and red channel information are required (Rouse, et al. 1973). However, for this purpose I used the near-infrared images of the area. Usually, the Canon

PowerShot SX260 HS camera provides images with a red, green and blue band. The modified version of the camera is producing images with near-infrared, green and blue band instead. Thus, the red band is not available in the pictures, taken by the modified camera.

To overcome this, I used the dual sensor approach, where images from the default camera and the modified camera are combined (Aber, Aber and Leffler 2001). I conducted the acquisition of the aerial images with the two respective cameras at different dates, but the UAV's flight paths were identical. Because I repeated the flight paths, I was able to capture identical aerial photographs of the study area from both cameras. Using the aerial images from both cameras, I created an orthomosaic from the combined multispectral images of the research area using Pix4Dmapper. This multispectral orthomosaic allowed using the red band channels of the default camera and the near-infrared band channels of the modified camera to compute the NDVI (Aber, Aber and Leffler 2001).

Comparison of DSM and NDVI

To investigate, whether there is a visible correlation between the calculated elevations and the calculated NDVI vegetation values, I compared the DSM and the NDVI images with each other. For this purpose, I isolated the highest reflectance values from the NDVI (representing vegetation) and projected them on the DSM to detect similarities visually (*Figure 19*).

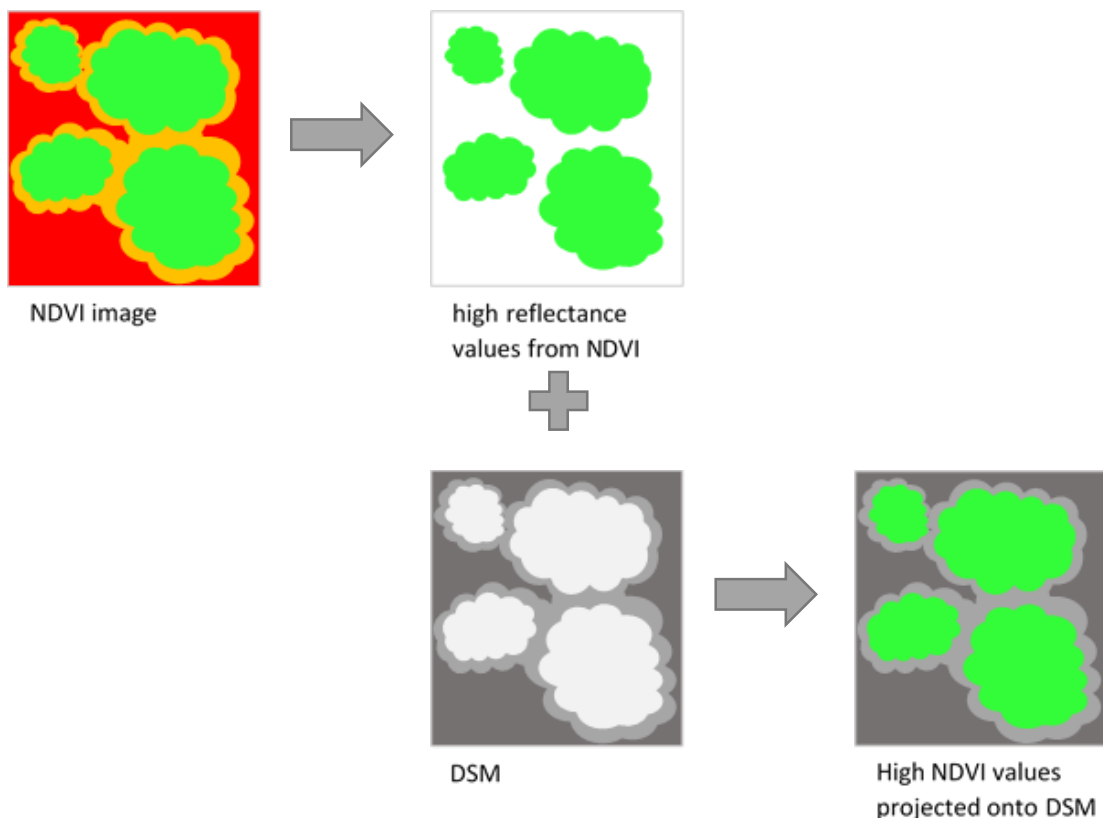


Figure 19. Schematic example of comparison of DSM with NDVI values. The simplified NDVI image shows a gradation from green (high values) to red (low values). The simplified DSM has a bright (elevation) to dark (depression) gradation.

Thematic Map

For the visualization of the landscape types and their varying characteristics, I developed a thematic map of the research area using QGIS. This allows for a simplified and generalized interpretation of the different landscape structures and facilitates an easier orientation and navigation in the field. For that reason, I used a visual classification approach. A visual image interpretation means to identify certain objects in the images based on the cognitive ability and experience of the human interpreter (Olson 1960). To identify objects and features, I considered image characteristics such as shape, size, pattern, tone and texture.

I used the generated orthomosaic of the research area as spatial reference. According to the occurrences in the study area, I divided the map into 13 categories:

- Oil palm plantation
- Oil palm plantation < 4 years
- Forest remnant
- Uncultivated land
- Recently deforested
- Orchard
- Building
- Wetland
- Water
- Path
- Stream
- Tree island
- Individual tree

Based on the thematic map, I calculated the sizes and percentages of the different classes of the research area with QGIS (version: Brighton 2.6.1).

Results

During two flights with an altitude of 300 m, the onboard camera of the UAV took a total of 880 images. Except for one image, I could calibrate all other 879 images (*Figure 38*, see Appendix) and used them for the development of the orthomosaic (*Figure 20*) and the corresponding DSM (*Figure 21*). This resulted in an average ground sampling distance of 9.37 cm. Like the DSM, the orthomosaic is displaying a total area of 628.096 ha.

Furthermore, I calculated the NDVI of the area using an orthomosaic generated with additional near-infrared information (*Figure 27*). To determine whether there is a correlation between NDVI values of vegetation and elevation, I combined and compared the DSM and the high reflectance values of the NDVI in *Figure 29*.

For a generalized overview of landforms and their distribution within the research area, I produced a thematic map (*Figure 31*) and calculated the percentages of the different areas (*Figure 30, Table 3, Table 4*).

Orthorectified Photomosaic

The orthorectified 2D photomosaic, generated with the Pix4Dmapper software, shows the entire area overflowed by the UAV (*Figure 20*). The total area amounts to 628.096 ha. In order to generate the orthomosaic, I used the same aerial pictures that generated the DSM. This means that the orthomosaic is also composed of images from two mission flights. It is composed of 879 aerial pictures and has an average ground sampling distance (GSD) of 9.37 cm. I saved the orthomosaic file as a TIFF with a size of 1.2 GB. I geometrically corrected the orthorectified photomosaic from distortions due to tilting of the camera during the UAV flight, distortions from the camera lens, and relief distortions. The orthomosaic displays all the information of a photograph, but additionally, true distances, angles and areas can be measured directly (Ayhan, et al. 2006).

Table 1. Calculated specifications of the orthomosaic

Total area	628.096 ha
Flight altitude	300 m
Number of images	879
GSD	9.37 cm



Figure 20. Orthorectified photomosaic of the research area

Digital Surface Model

I generated the digital surface model (DSM) by compiling the aerial photography with the Pix4Dmapper software. It shows a 3D representation of the areas' surface, overflowed by the UAV with two missions (*Figure 21*). For the reconstruction of the DSM, the software recognized an average of 23,546 keypoints per image. The calculated elevations vary from a minimum of 26.498 m to a maximum of 89.033 m above sea level. The average altitude is 52.809 m above sea level. I calculated the altitude values for the total area of 628.096 ha. For the visualization of the elevations, I applied a colored gradation to the DSM, using QGIS.

Table 2. Calculated specifications of the DSM

Total area	628.096 ha
Max. altitude	89.033 m
Min. altitude	26.498 m
Mean altitude	52.809 m
Median keypoints per image	23 546

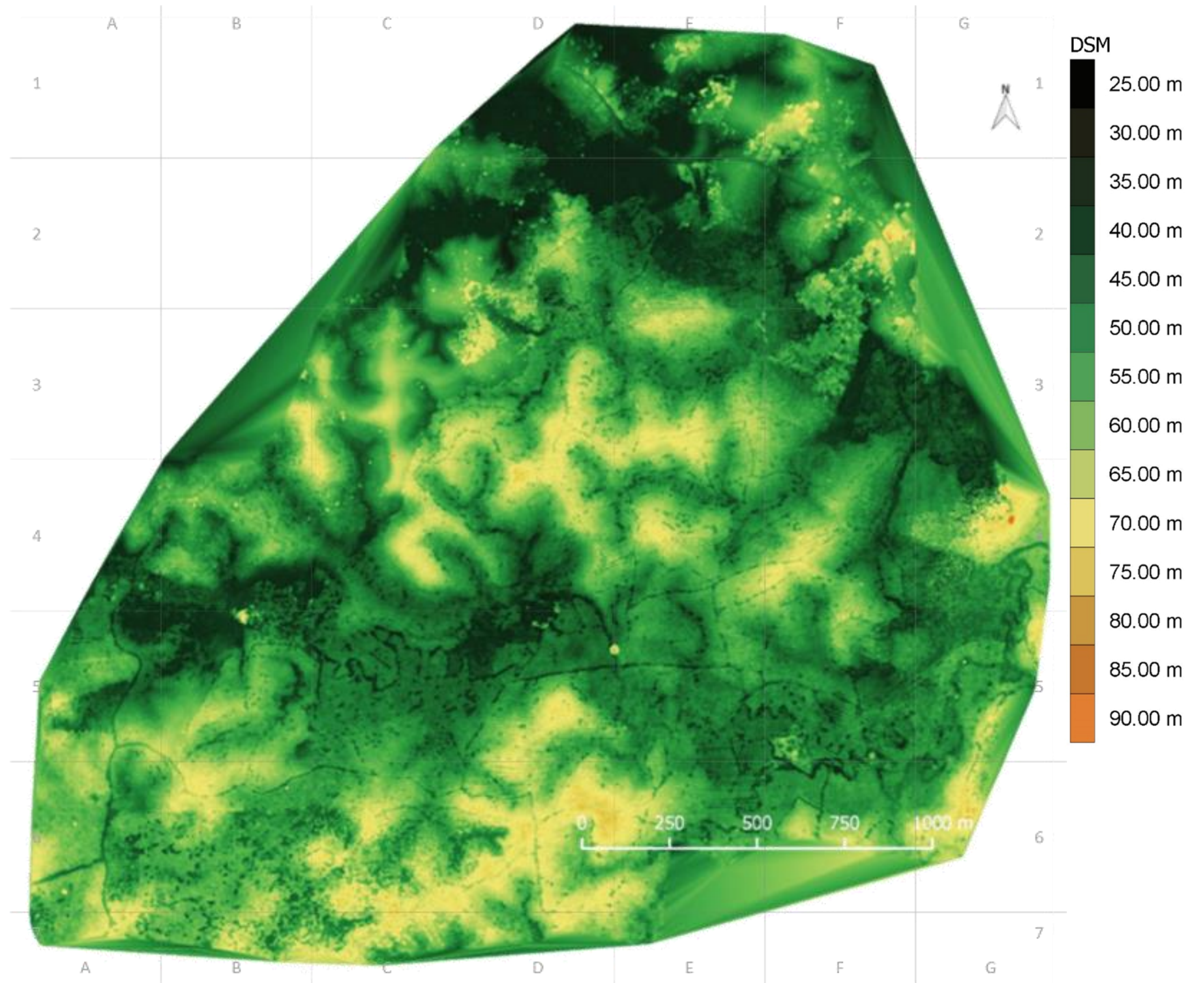


Figure 21. Digital surface model of the research area

Correlation of Altitudes

The calculated correlation between altitudes derived by GPS-unit on the ground and calculated through photogrammetric processes with data from UAV flights:

$$\text{cor.} = 0.09383896$$

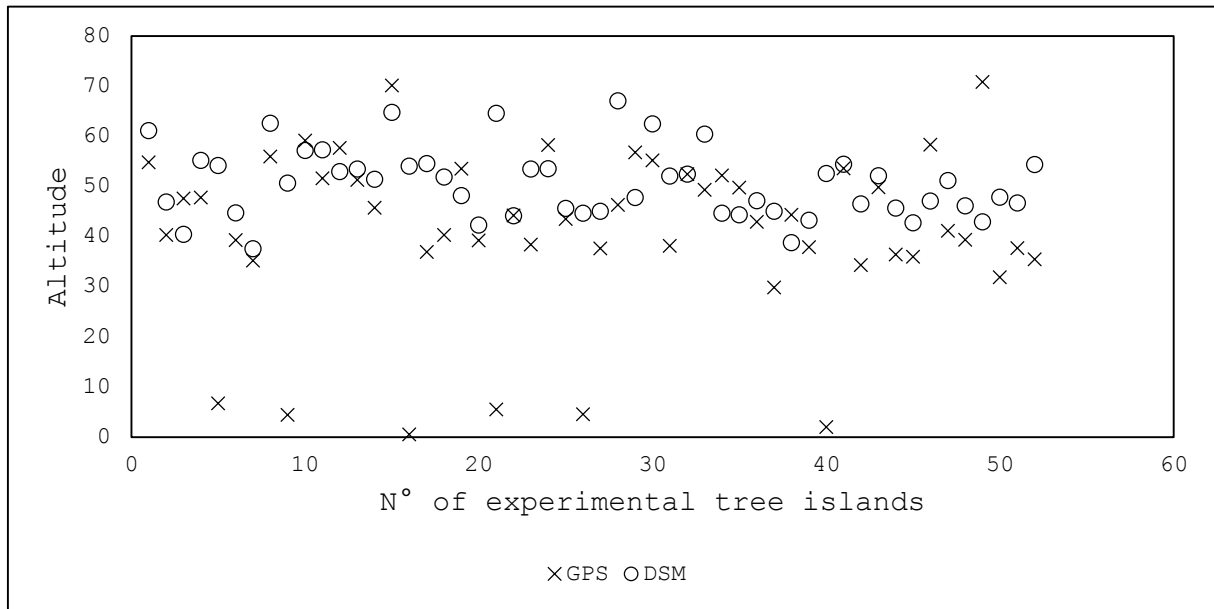


Figure 22. Correlation of altitudes, including all measurements

However, certain altitude values from the GPS device appeared incorrect. Either they showed values higher than those of the DSM, or they indicated an altitude less than 10 m above sea level. When I excluded the incorrect values from the calculation, the correlation result is:

$$\text{cor.} = 0.709202649$$

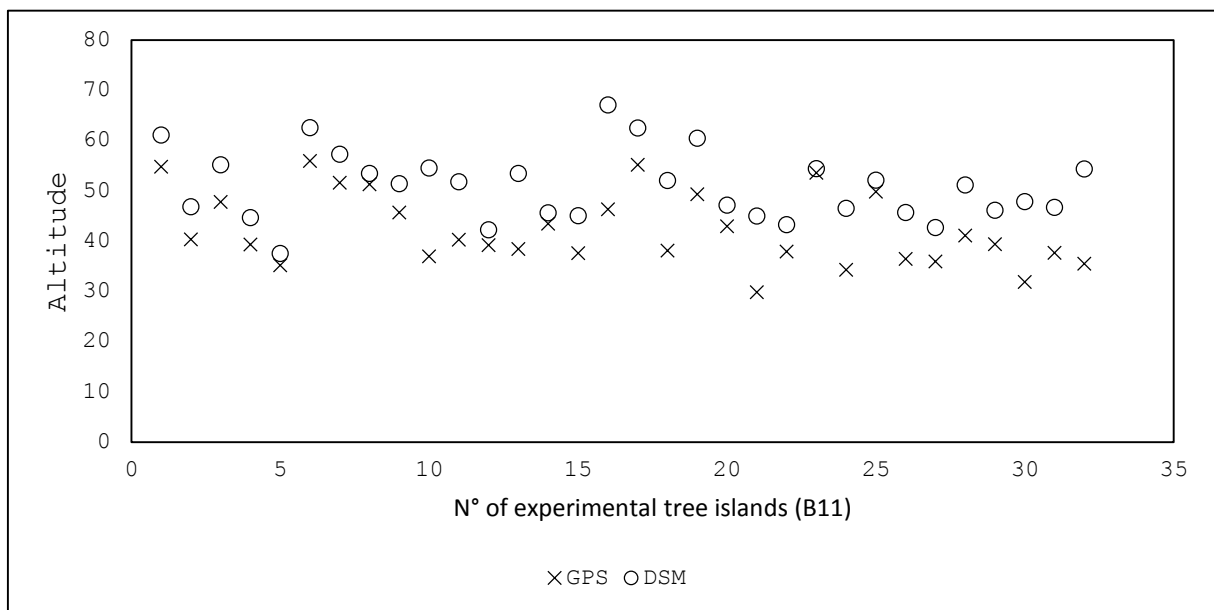


Figure 23. Correlation of altitudes, excluding incorrect measurements

Normalized Difference Vegetation Index



Figure 24. Orthorectified photomosaic of the research area, with NIR, green and blue color channels

Figure 24 is showing the orthorectified photomosaic of the near-infrared pictures and *Figure 27* is illustrating the calculated NDVI color map. Due to malfunctioning of the camera in the last three transects of the flight path, a small area of northern part of the research area is missing (*Figure 25*). However, I was able to calculate results for the majority of the area. The NDVI values vary from -0.81 to 0.71. For visualization, I categorized the values in five classes (*Figure 26*):

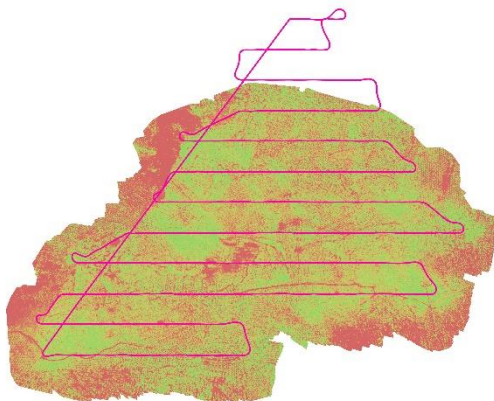


Figure 25. Illustration of the missing northern part

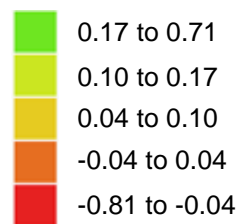


Figure 26. Five classes of the NDVI color map

The stronger the green color, the higher the reflectance of near infrared light in the corresponding image section. The NDVI color map allows to clearly distinguish between vegetation and non-vegetation. The values from -0.81 to 0.10 are displaying water, soil, shade and buildings, whereas vegetation is represented by the values from 0.10 to 0.71.

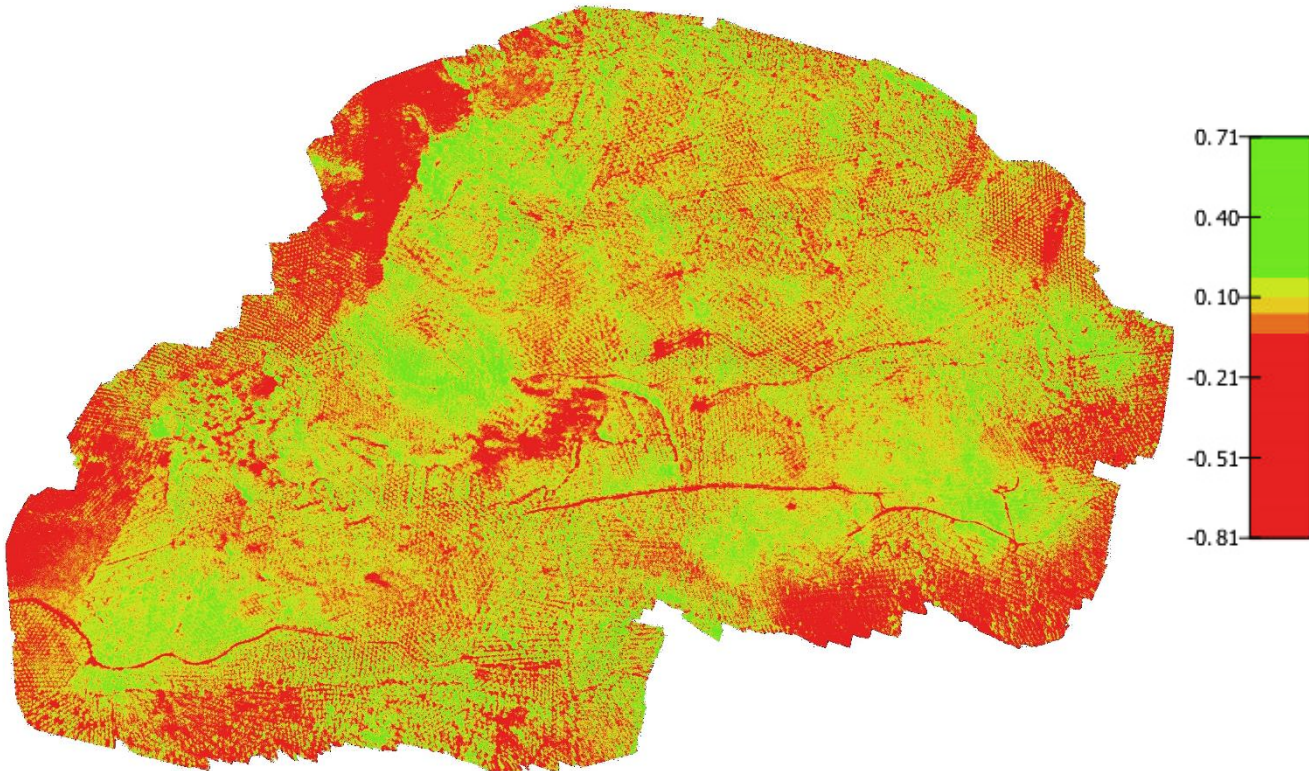


Figure 27. Color map of calculated NDVI

Comparison of DSM and NDVI

To determine, whether there is a correlation between NDVI values of vegetation and elevation, I combined and compared the DSM and the NDVI values from 0.17 to 0.71 (Figure 29). For this, I projected the NDVI values onto the elevation model. I found a visual relationship between the reflectance and the DSM (Figure 28). It appears that depressions, west to south-west oriented slopes and waterbodies show a stronger reflectance in the near-infrared spectral range, than the rest of the research area.

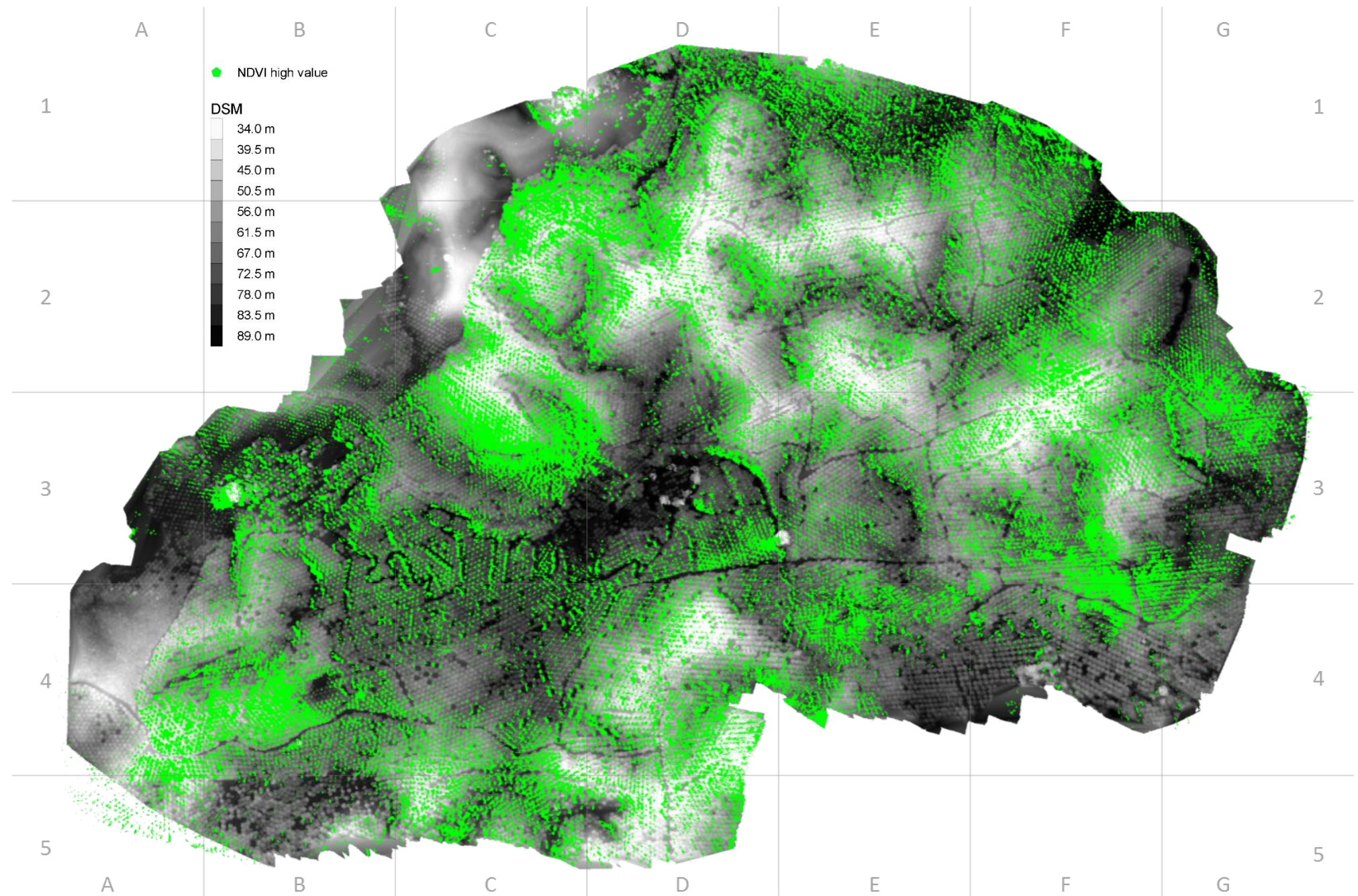
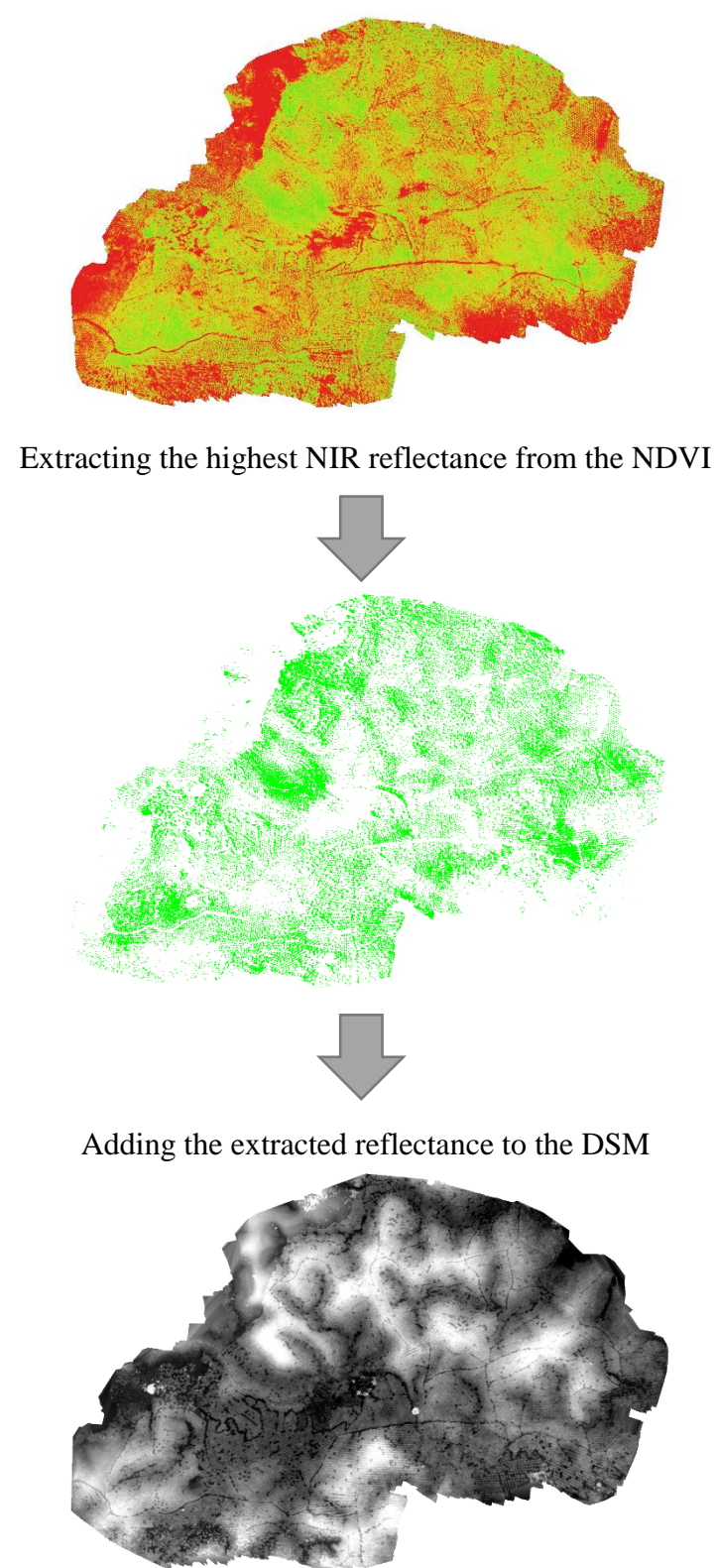


Figure 29. Grey scale DSM overlaid with the highest reflectance values of the NDVI

Figure 28. Schematic description of the comparison

Thematic Map and Area Distribution

I produced a thematic map for the complete area (*Figure 31*). This map displays the areal distribution of the research area based on the orthomosaic. I visually categorized the map into 13 classes (*Figure 31, Figure 32*). The areal size of the individual classes and their percentage of the total area are presented in Table 3 and Table 4. In addition, I integrated 43.82 km of paths, 15.83 km of streams and 19 individual trees outside the forest remnants into the map. I also displayed the distributional percentages of different landform types in the area in a pie chart (*Figure 30*). For a clearer illustration, I subdivided the pie chart into oil palm plantations, forest remnants, uncultivated land, orchards, tree islands (representing the survey plots of the B11 project) and water.

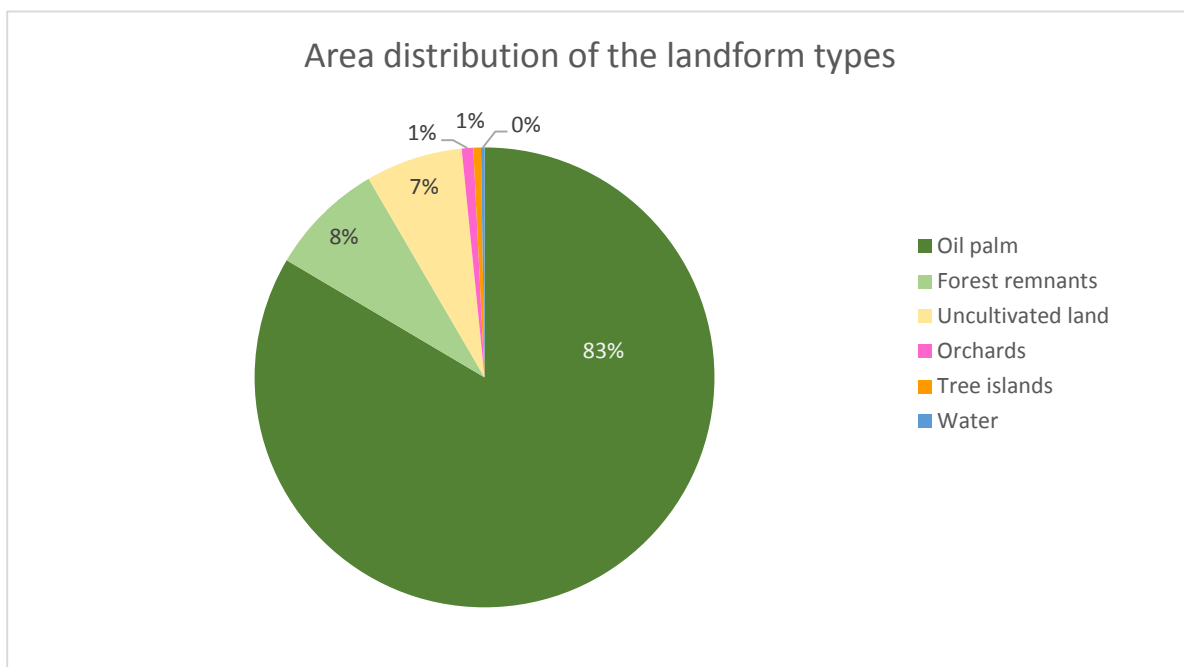


Figure 30. Pie chart of the area distribution within the research area

Table 3. Distribution and size of areas within the research area according to the pie chart

	Area m ²	Area ha	Percent
Oil palm	5,207,970	521	83.5 %
Forest remnants	504,080	50	8.1 %
Uncultivated land	425,328	43	6.8 %
Orchards	50,562	5	0.8 %
Tree islands	33,150	3	0.5 %
Water	15,405	2	0.2 %
Total	6,236,495	624	100 %

Table 4. Distribution and size of areas within the research area according to the thematic map

Layer	Area m ²	Area ha	Percent
Oil palm	4,866,819	486.68	78.0 %
Oil palm < 4 yrs	341,151	34.12	5.5 %
Forest remnants	504,080	50.41	8.1 %
Uncultivated land	401,755	40.18	6.4 %
Recently deforested	12,059	1.21	0.2 %
Water	12,669	1.27	0.2 %
Wetland	5,817	0.58	0.1 %
Orchards	50,562	5.06	0.8 %
Building	11,515	1.15	0.2 %
Tree islands	33,150	3.32	0.5 %
Total	6,239,577	623.96	100 %

Legend

- Oil palm
- Oil palm (< 4 yrs.)
- Forest remnant
- Orchard
- Uncultivated land
- Wetland
- Recently deforested
- Water
- Stream
- Path
- Building
- Tree island
- Individual tree

Figure 32. Legend of the thematic map

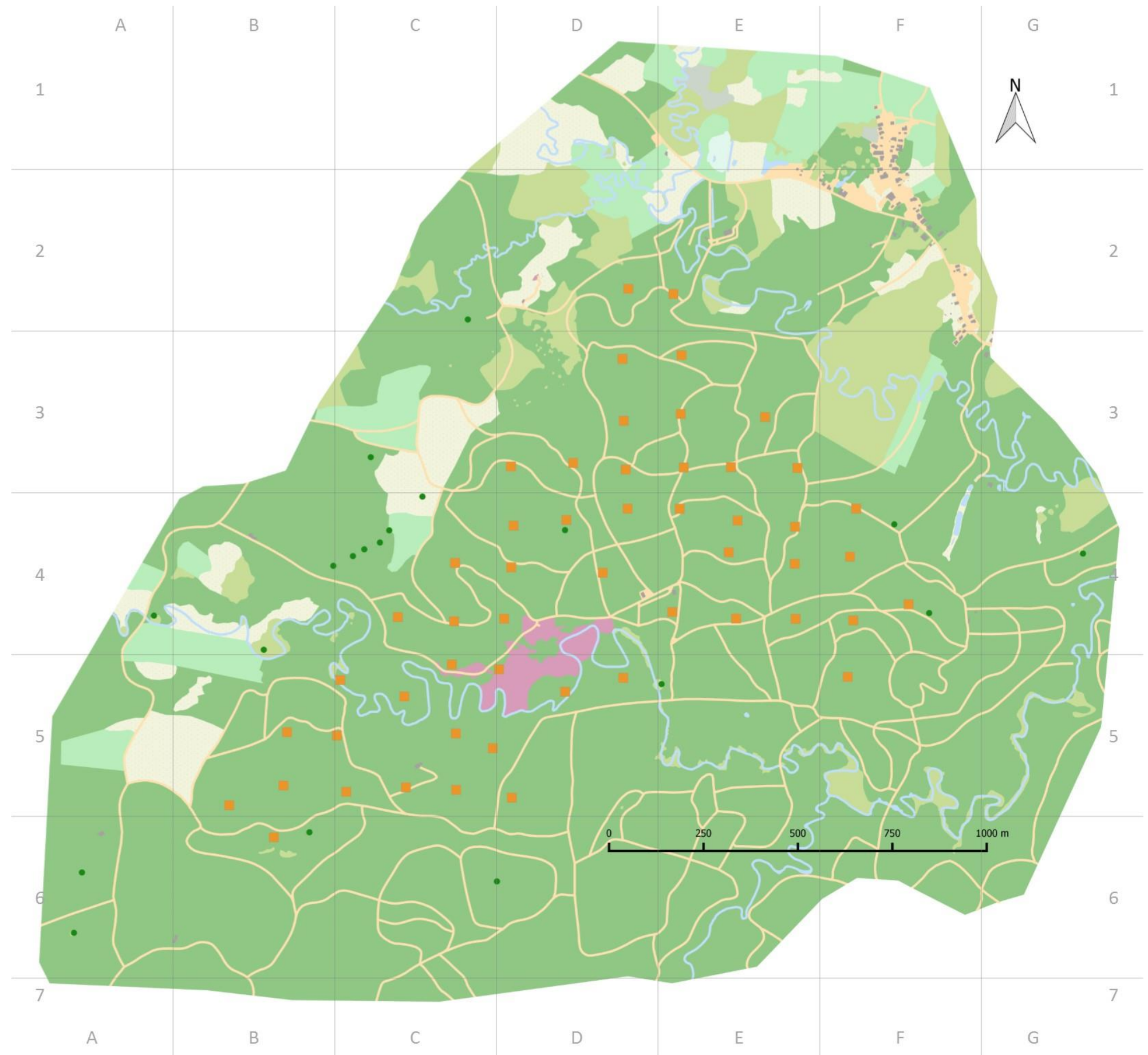


Figure 31. Thematic map of the research area

Discussion

The purpose of this thesis was to assess the implementation of a low-cost UAV in tropical conditions. The UAV was equipped with compact system cameras, capable to record photographs in VIS and near-infrared light. Through photogrammetry, I generated an orthorectified photomosaic (*Figure 20*) and a digital surface model (*Figure 21*). Furthermore, I used the aerial near-infrared pictures to calculate the NDVI (*Figure 27*). Based on the orthomosaic, I created a thematic map of the research area (*Figure 31*). The results emphasize that an UAV indeed can be an appropriate and reliable tool in the field of tropical forest ecology.

Evaluation of Methods

The application of UAVs in the field of ecology is still in an early stage of development and pursues different approaches. According to Chandler (1999), it is recommended to use ground control points (GCP) to increase the geographical accuracy of the generated orthomosaic. These GCP appear on the aerial pictures and their exact GPS locations are known. Usually, they are premarked artificial features, whose coordinates have to be determined in the field (d'Oleire-Oltmanns, et al. 2012). In contrast, Küng, et al. (2011) point out that it is possible to create orthorectified photomosaics without the utilization of GCP. The geo-localization process without GCP depends on the recorded GPS measurements provided by the autopilot during UAV flights. Depending on the application, the burden of measuring GCP can be traded against a lower resulting accuracy (Küng, et al. 2011). During the implementation of this thesis' scope, I deliberately chose to omit GCP. The purpose of this study was to enquire and emphasize a UAV application, with focus on tropical forest ecology. In the tropics, areas of interest are often difficult to access and sometimes even completely unexplored. Under these conditions, setting up GCP can be very time and labor intensive. To avoid that effort, I neglected the minor loss of accuracy and did not install GCP in the area. The resulting orthorectified photomosaic shows an average ground sampling distance of 9.37 cm (*Table 1*), which is sufficient for most requirements.

However, a decisive criterion is the overlap of the aerial images. Sufficient side and frontal overlap are crucial for the successful development of an orthorectified photomosaic (Küng, et al. 2011). The side overlap also defines the travelled distance during a mission. The greater the side overlap within pictures, the longer the total distance becomes (and vice versa) to cover an identical area (*Figure 9*). In order to cover as much area in one mission as possible, I chose a relatively small side overlap of 50 % (see page 20), as recommended by the aerial data

collection guidelines provided by Drone Mapper (2012). This overlap setting was sufficient to process the aerial pictures recorded at 300 m altitude (*Figure 36, Figure 37, Figure 38*; see Appendix). However, the overlap at lower altitudes must be much larger. Otherwise, the pictures cannot be processed due to the increased perspective. An object, which is two times closer to the camera than another, will appear four times larger in the picture (O. Küng, Pix4D Webinar 1: Introduction to Modern Photogrammetry and Optimal Flight Plans 2014). This effect increases, when the altitude decreases and a ‘façade problem’ may occur (O. Küng, Pix4D Webinar 1: Introduction to Modern Photogrammetry and Optimal Flight Plans 2014). A camera would photograph objects rather from the side and not directly from above, if the provided overlap were set too low (*Figure 33*). This makes it impossible to merge individual

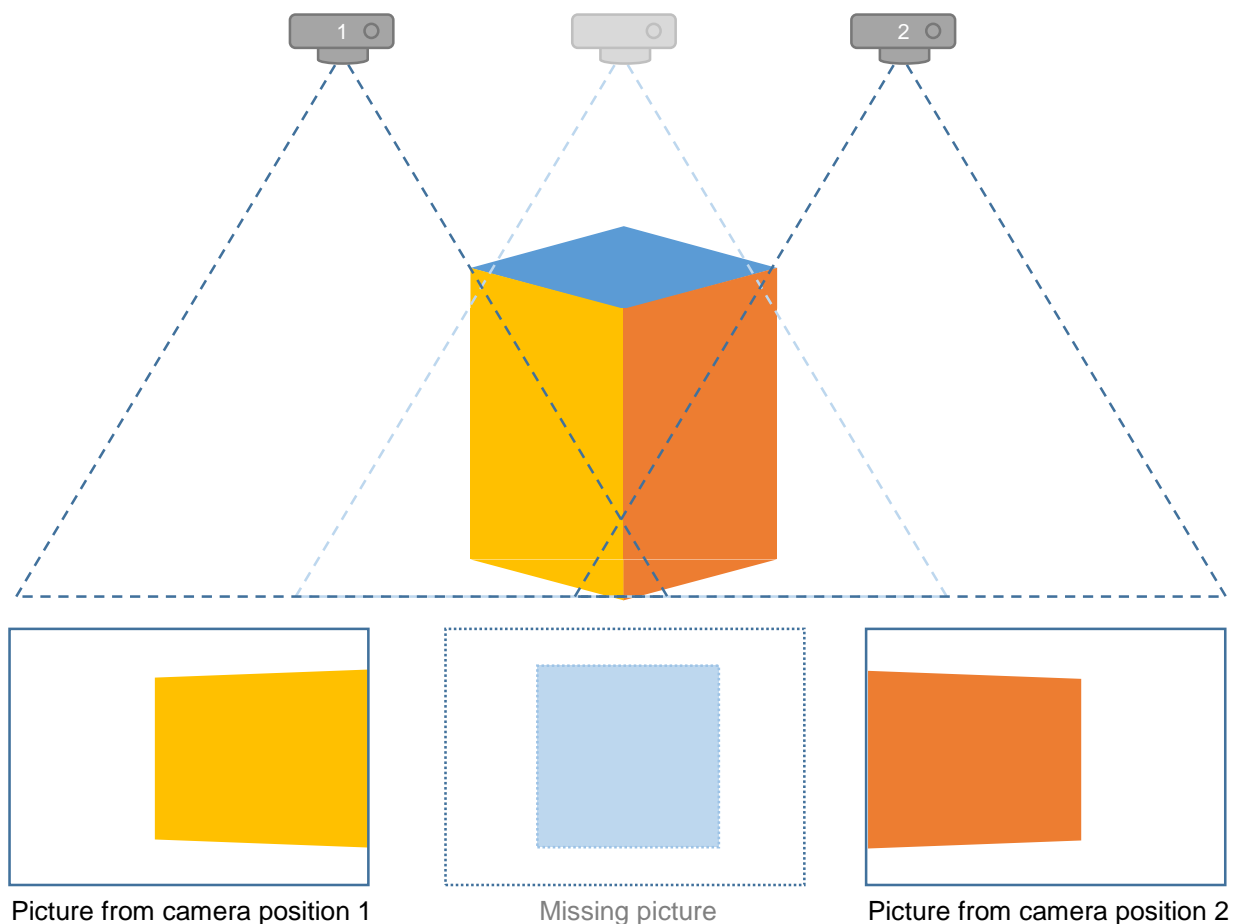


Figure 33. Schematic illustration of the 'Façade problem', due to insufficient overlap

images correctly. To compensate the increasing perspective and to avoid the ‘façade problem’, Pix4D recommends a frontal overlap of at least 85 % and a side overlap of 75 % in lower altitudes (O. Küng, Pix4D Webinar 1: Introduction to Modern Photogrammetry and Optimal Flight Plans 2014).

Despite the relatively small overlap of 50 % for the missions at 300 m altitude, it was sufficient to generate the presented results. In Figure 36 (see Appendix), the connections of the displayed individual images show that most pictures overlap frontal and not sideways. This is caused by the compromise to cover as much area in one flight as possible and the choice of a small overlap. From 880 recorded aerial pictures, I could use 879 pictures for orthorectification and to produce the results. The green coloration in Figure 37 (see Appendix) confirms a sufficient overlap. Only at some parts on the edge of the figure, a red coloration is indicating an insufficient overlap that manifests in minimal distortions.

Orthorectified Photomosaic

During flight, the UAVs onboard camera provides a multitude of aerial pictures. Through photogrammetric processes, I was able to compose these picture data sets to one large photomosaic, displaying a map of the overflown area. The resulting orthorectified 2D photomosaic map (*Figure 20*) allows a general overview of the entire experimental area and surroundings (628 ha) in its present state.

Comparing an orthorectified photomosaic to a non-orthorectified image merging process, the main advantages is the correction for distortions due to tilting of the camera during the UAV flight, distortions from the camera lens and relief distortions. An orthomosaic displays all information of a photograph, but additionally true distances, angles and areas can be measured (Ayhan, et al. 2006). The ground sampling distance (GSD) of 9.37 cm (*Table 1*) allows for accurate identification and interpretation of vegetation features and objects (Landsat 8 imagery, for comparison, has a GSD of 30 m (USGS 2014)). Due to the regular planting and their star-shaped crown, researchers can easily distinguish the oil palms from other forms of vegetation. The dense appearance of oil palms in the orthomosaic shows the proliferation of these monocultures in this region. This became particularly evident, when I used freely available satellite imagery from the past years for comparison (*Figure 35 and Figure 34*).



Figure 35. Satellite image of the research area (Google Earth, 2007)



Figure 34. Orthorectified photomosaic of the research area (2014)

The different colorations, for example in the grid squares C4, D2 and F5 (*Figure 20*), are caused by changes in light conditions that inevitably occur, when clouds move in front of the sun. Under sunny conditions, pictures will have a lot of contrast, due to hard shadows and bright spots. If it is cloudy, pictures will appear more flat and darker.

However, other forms of vegetation are visible in the orthomosaic. For example, forest remnants (e.g. in grid square F3) and orchards (e.g. in grid square D4) are recognizable in *Figure 20*. Apart from the different vegetation types and streams, infrastructural facilities such as roads, buildings and settlements (e.g. in grid square F2, *Figure 20*) are identifiable as well.

Digital Surface Model

The digital surface model (DSM) is an elevation model that represents the surface of the research area. I calculated its altitudes through aerial photogrammetry, a measurement method determining the position and spatial extent of objects, based on photographic images (see page 30). A DSM does not represent the topography, but the surface structure of the ground. This means that a planar surface may have different elevations in the model, due to different levels of vegetation height. For example, on a plane, the canopy of a forest is higher than of a meadow landscape. Within the area, the altitude varies approximately between 25 m and 90 m above sea level, according to the DSM (*Figure 21*). The majority of the area is cultivated with oil palm monocultures (*Figure 30*). The age of these monocultures is almost identical and fluctuations in height growth are therefore very small. The oil palms in the plantation of the the B11 research area are reaching an average height of about 2 – 9 m (Röll, et al. In preparation). This means that height differences of newly planted oil palm trees and mature oil palms trees relate to a maximum of 9 m and those height deviations in the DSM to the ground surface can reach a maximum of 9 m. Moreover, accumulations of forest remnants (in total 8.1 %, *Table 3*) are visible in the research area. However, their crown surfaces also show a relatively uniform height (*Figure 21*).

Nevertheless, the DSM can be used to estimate the topography, as due to the reasons stated above, the influence of vegetation heights appear to be minor in comparison to the terrain elevations. The colored representation of heights changes from black to green and beige to orange (*Figure 21*). The pixels with the lowest elevation value are displayed in black and the pixels with the highest elevation values correspond to orange. In the DSM, especially single freestanding or superior trees are clearly observable. Due to the abrupt differences in height, the color of the tree canopies is differing strongly from its vicinity. I assume that these

individual trees (e.g. in grid squares B5, C3, D/E5 and G4 of the DSM, *Figure 21* and the orthomosaic, *Figure 20*) are leftovers from the former tropical forest.

Correlation of Altitudes

Considering the correlation values between the altitudes of the GPS data and the photogrammetric data, I noticed how far they differ. A correlation value of 0.09 (see ‘Correlation of Altitudes’ at page 38) is very low and indicates almost no relationship (Oestreich and Romberg 2014). However, I assume that certain values of the GPS device are incorrect, because they either showed values higher than those of the DSM, which cannot be true as the DSM is derived from top surfaces. Furthermore, certain GPS values indicate an altitude less than 10 m above sea level, which can also not be true as the lowest altitude is 26.5 m (*Table 2*), based on the assumption that the photogrammetric altitude values are more precise than the GPS device.

When I excluded the values that I assumed to be incorrect (*Table 8*, see Appendix) from the calculation, the correlation value is 0.71 (see page 38). As it is close to 1, a fairly strong relationship between the two altitude data is suggested (Oestreich and Romberg 2014). It seems that the photogrammetric calculated altitudes are correct and reliable. However, a high correlation between two data sets does not imply that the two variables have a high causality. Instead, the correlation only provides a first indication, that this might be the case (Oestreich and Romberg 2014). Thus, it seems that the GPS device is less precise than the photogrammetric measurements.

Normalized Difference Vegetation Index

Using the recorded images from the default and the modified Canon PowerShot SX260 HS camera, I calculated the ‘normalized difference vegetation index’ (NDVI) for the research area. The NDVI highlights the difference between the red and infrared wavelengths that the vegetation reflects. Plants use red light, but not infrared light for photosynthesis, so the NDVI allows determining the vitality of green vegetation (see page 15).

Healthy vegetation will absorb most of the visible light for energy production. However, the foliage’s chlorophyll reflects a large portion of the near-infrared light. Unhealthy or sparse vegetation reflects more of the visible light and less near infrared light, because the chlorophyll content is lower. The larger the difference between the near-infrared light and the red light reflectance of an area, the more chlorophyll there has to be (see page 32) (Rouse, et al. 1973). Theoretically, NDVI values are represented as a ratio ranging from -1 to 1, but in the resulting

NDVI color map, the values range between -0.81 and 0.71 (*Figure 27*). I categorized these values into five classes (*Figure 26*). The first three classes ranging from -0.81 to 0.10 are representing water, soil, shade and buildings, whereas the area's vegetation is represented by values from 0.10 to 0.71. Because the near-infrared pictures for the NDVI are derived from a custom modified digital camera, the results should be interpreted with caution, as modified cameras can lead to inaccurate results, when they were not calibrated professionally (Ritchie, et al. 2008). The values and ranges of the obtained NDVI are most likely differing from those obtained from a professional multispectral camera, as camera sensors do have different near-infrared widths. Depending on the variability of vegetation stress, a low spectral range camera would not detect small variations, whereas a professional near-infrared camera is more sensitive (Ritchie, et al. 2008). Nevertheless, a modified camera can produce good practical results at low costs (Dvolarai and Alexandre 2014).

The white balance is a critical factor, to receive good NDVI data from modified cameras. According to Public Lab (2013), the white balancing was conducted properly, when infrablue pictures of healthy plants appear orange yellow. This corresponds to the resulting infrablue orthomosaic (*Figure 24*), which suggests that the white balance of the camera was set correctly.

If I consider the highest reflection values from the NDVI in isolation and project them onto the elevation model (*Figure 29*), I conclude on a relationship between height and light reflection in the near-infrared light. In the DSM, a bright color scheme indicates an elevation and a dark color scheme indicates a depression. Green areas show a high reflection of infrared light that indicate a generally vigor vegetation, due to a higher chlorophyll accumulation in these specific areas. Regarding the region around the grid squares C2 to F2 in *Figure 29*; I noticed that the vegetation with the highest proportion of reflection mainly concentrates in depressions and valleys. In contrast, elevations (recognizable by the bright coloring) exhibit a lower occurrence of green spots. This observation seems consistent with the topography aspect and the accompanying sun exposure.

Oil palms require a relatively stable high temperature throughout the year. A high level of solar radiation of five to seven sunshine hours per day is important for an optimal growth. Furthermore, an almost continuous moisture supply is a critical factor of oil palm growth and moisture deficits affect the vitality of oil palms (Verheye 2010). Hilltops do not seem to fulfill these environmental requirements completely. The conditions for oil palm trees appear to be rather favorable in depressions, because the water flows downhill and so the soil moisture on hilltops fades away faster. In contrast, the run-off water from higher locations improves the

water supply in lower areas. Considering the grid square C3 (*Figure 29*), I also assume that a southwest slope orientation in combination with better water availability is offering better growth conditions for oil palms. Presumably, an optimal exploitation of the daily solar radiation favors the growth conditions. Water availability generally seems to have a positive impact on the vegetation vitality in this region, which seems to be improved along streams, for example in grid square B3 of *Figure 29*.

Thematic Map

As a further result, I produced a thematic map by visual interpretation of the orthorectified photomosaic (*Figure 31*). This map is a simplified representation of the area. Through generalization and structuring, the different local characteristics become easier to read. Since the thematic map is based on the orthomosaic, it is true to scale. Therefore, it is possible to read off measurements of distances, angles, and areas precisely. The planted oil palms occupy the majority of the area. I decided to split the oil palm plantations into two categories: oil palm plantations younger than four years and oil palm plantations older than four years. As young oil palms have not formed a closed canopy yet, I could easily identify them (Breure 2010). The mature oil palms claim 78 %, whereas the young oil palms make up 5.5 % of the total area. Together, they occupy 83.5 % of the area (*Table 4*). Covering 8.1 %, forest remnants represent the second most common type of vegetation (*Table 4*). In total, I detected 12 individual, non-contiguous forest remnants within the research area. However, I do not consider these forest remnants as undisturbed, because they are directly exposed to humans and are located next to oil palm plantations. The forest remnants are rather degraded leftovers of the former tropical lowland rainforest. Nevertheless, forest remnants as well as the remaining individual trees within the plantation area fulfill important ecological functions. They represent a remaining seed source, promote natural regeneration, improve biodiversity and serve as shelter for wildlife. However, the thematic map was developed by the visual interpretation of the orthomosaic. Therefore, this is only a rough assessment. In order to have absolute data, the thematic map should be counterchecked with other data.

Conclusion

Based on the results I provided, researchers can derive a lot of information and use them for the ongoing B11 project, especially since they are near real-time up to date. The results can be used to measure straight-line distances between tree island survey plots and potential seed sources, the elevation structure of the environment can be easily estimated and due to the high ground sampling resolution of 9.37 cm of the orthomosaic, small details can be recognized and many insights can be gained. As the application of low-cost UAVs in the field of ecology is a relatively new approach, researchers need to continue to explore the full potential of UAVs furthermore.

In summary, this thesis confirms that researchers can successfully apply UAVs to investigate and monitor tropical regions. UAVs are reliable and cost-effective tools for skilled researchers that can use the obtained aerial imagery to generate orthorectified photomosaics, DSM and to calculate the NDVI for large areas. In general, UAVs are a valuable instrument in the field of ecology and environmental remote sensing. For the exploration of inaccessible and remote areas, the use of UAVs is less time consuming, less labor intensive and more cost effective than ground surveys. As the provided data are near real-time, UAVs can continuously monitor changes in landscapes (e.g. logging, fires, afforestation and crop development). The application of low-cost UAVs in the field of tropical forest ecology is still in an early stage of development. UAVs could be revolutionizing natural science; similar to those transformations that GIS and GPS brought two decades ago (Watts, Ambrosia and Hinkley 2012). With constant technological progress, increasingly affordable prices and an adapted legislation, UAVs will become more popular and continue to play an important role in the future.

References

- 3DR. "3drobotics: wp content: uploads: RTF Checklist." *3D Robotics*. 2014. www.3drobotics.com (accessed May 20, 2014).
- . "Products: Aero." *3D Robotics*. 2014. www.store.3drobotics.com/products/3DR-Aero (accessed April 2014).
- . "Support: Aero-M: Operation Manual." *3D Robotics*. 2015. www.3drobotics.com/aero-m/ (accessed February 1, 2015).
- Aber, James S., Susan W. Aber, and Brooks Leffler. "Challenge of Infrared Kite Aerial Photography." *Transactions of the Kansas Academy of Science*, 2001: 18-27.
- APM. *APM Multiplatform Autopilot*. 2014. www.ardupilot.com (accessed February 15, 2015).
- Ayhan, Eminnur, Özlem Erden, Gülçin Atay, and Esra Tunç. "Digital Orthophoto Generation with Aerial Photos and Satellite Images and Analyzing of Factors which Affect Accuracy." *Shaping the Change XXIII FIG Congress*. Munich, Germany, 2006.
- Breure, C.J. "Rate of leaf expansion: A criterion for identifying oil palm (*Elaeis guineensis* Jacq.) types suitable for planting at high densities." *NJAS - Wageningen Journal of Life Sciences*, June 2010: 141-147.
- Canon. *Cameras: Canon PowerShot SX260 HS*. 2014. www.canon-europe.com (accessed April 2014).
- Chandler, Jim. "Effective Application of Automated Digital Photogrammetry for Geomorphological Research." *Earth Surface Processes and Landforms*, 1999: 51-63.
- CHDK. *Home: Professional control*. 2014. www.chdk.wikia.com (accessed May 7, 2014).
- CRC 990. *Collaborative Research Centre 990: Ecological and Socioeconomic Functions of Tropical Lowland Rainforest Transformation Systems (Sumatra, Indonesia)*. 2012. www.uni-goettingen.de (accessed March 2014).
- d'Oleire-Oltmanns, Sebastian, Irene Marzolf, Klaus Daniel Peter, and Johannes Ries. "Unmanned Aerial Vehicle (UAV) for Monitoring Soil Erosion in Morocco." *Remote Sensing*, November 7, 2012: 3390-3416.

- Drone Mapper. "Documentation: Support: Aerial Data Collection Guidelines & Flight Planning." *Drone Mapper*. 2012. www.dronemapper.com (accessed June 2014).
- Dvolarai, W., and S. Alexandre. "LinkedIn: Discussion: Precision Agriculture: Remote Sensing: UAV." March 17, 2014.
- Hanusch, Thomas. "Grundlagen und Prinzipien der Photogrammetrie und Fernerkundung." *Photogrammetry remote sensing*, Swiss Federal Institute of Technology Zurich, Zurich, 2010.
- Harvey, Phil. 2012. www.sno.phy.queensu.ca (accessed August 28, 2014).
- Jones, Hamlyn G., and Robin A. Vaughan. *Remote sensing of vegetation – Principles, techniques, and applications*. New York: Oxford University Press, 2010.
- Koh, Lian Pin, and Serge A. Wich. "Dawn of drone ecology: low-cost autonomous aerial vehicles for conservation." *Tropical Conservation Science*, July 9, 2012: 121-132.
- Küng, O., A. Beyeler, J-C. Zuffery, D. Floreano, P. Fua, and F. Gervais. "the Accuracy of Automatic Photogrammetric Techniques on Ultra-Light UAV imagery." *Unmanned Aerial Vehicle in Geomatics*. Zürich, CH: École Polytechnique Fédéral de Lausanne, 2011.
- Küng, Oliver. *Pix4D Webinar 1: Introduction to Modern Photogrammetry and Optimal Flight Plans*. Pix4D. June 23, 2014. www.support.pix4d.com (accessed March 11, 2015).
- Main, Carlyn. *Science Tech: Models & Replicas: Model Airplane Review: Tips for Flying Radio Controlled Model Airplanes*. 2014. www.model-airplane-stores-review.toptenreviews.com (accessed July 6, 2014).
- Minnesota Department of Natural Resources. *DNRGPS Application*. 2015. www.dnr.state.mn.us (accessed September 02, 2014).
- Mitchell, Dave. *Zenoshrdlu: Simple Tool for Installing CHDK*. August 24, 2013. www.zenoshrdlu.com (accessed April 12, 2014).
- Oestreich, Markus, and Oliver Romberg. *Keine Panik vor Statistik*. 5. Wiesbaden: Springer Spektrum, 2014.

- Olson, C.E. "Elements of photographic interpretation common to several sensors."
Photogrammetric Engineering, 1960: 651-656.
- Pix4D. *Support: Knowledge Base*. 2015. www.pix4d.com (accessed February 03, 2015).
- Public Lab. *Public Lab: Superblue*. 2013. publiclab.org (accessed June 2014).
- QGIS. *For Users: Download QGIS*. 2015. www.qgis.org (accessed August 01, 2014).
- Ritchie, G.L., D.G. Sullivan, C.D. Perry, J.E. Hook, and C.W. Bednarz. "Preparation of a low-cost digital camera system for remote sensing." *Applied Engineering in Agriculture*, 2008, 24 ed.: 885-896.
- Röll, Alexander, et al. *Transpiration in an oil palm landscape: effects of palm age*. In preparation.
- Rouse, J.W. Jr., R.H. Haas, D.W. Deering, and J.A. Schell. *Monitoring the vernal advancement and retrogradation (green wave effect) of natural vegetation*,. Greenbelt, Maryland: Texas A&M University Remote Center, 1973.
- Schmidt, Friedemann. *Home: Downloads*. 2011. www.geosetter.de (accessed September 24, 2014).
- Škiljan, Irfan. *Home: Downloads*. 2014. www.irfanview.de (accessed July 05, 2014).
- Taylor, Jeff. *Home: 2013: August: 24: Infrablue Conversion to Record Vegetation Stress on an SX260*. August 24, 2013. www.droneyard.com (accessed March 15, 2014).
- USGS. *Home: Frequently Asked Questions about the Landsat Missions* . 2014. landsat.usgs.gov (accessed March 29, 2015).
- Verheye, Willy. "Growth and production of oil palm." In *Land Use, Land Cover and Soil Sciences. Encyclopedia of Life Support Systems (EOLSS)*. Oxford: UNESCO-EOLSS Publisher, 2010.
- Watts, Adam C., Vincent G. Ambrosia, and Everett A. Hinkley. "Unmanned Aircraft Systems in Remote Sensing and Scientific Research: Classification and Considerations of Use." *Remote Sensing*, June 8, 2012: 1671-1692.

Appendix

Table 5. Specification of the Canon PowerShot SX260 HS digital camera (Canon 2014)

Features	Description
Image sensor	1/2.3" type back-illuminated CMOS
Sensor Width	6.17 mm
Sensor Height	4.55 mm
Effective Pixels	12.1 MP
Image Processor	DIGIC 5 with iSAPS technology
Focal Length	4.5 – 90.0 mm (35 mm equivalent: 25 – 500 mm)
GPS	Yes
Image Recording Format	JPEG
Battery Type	Canon NB-6L Li-ion battery
Weight	Approx. 231 g (including battery/batteries and memory card)
Dimensions (WxHxD)	106.3 x 61.0 x 32.7 mm

Table 6. Specifications of the UAV (3DR, 2014)

Features	Description
Aircraft dimensions	188 cm wingspan, 129 cm length
Aircraft weight with battery	3 kg
Payload capacity	2 kg
Autopilot system	Pixhawk flight controller
Motor	RC Tiger Motor 2820 830 kV
Propeller	Gemfan 11" x 7"
Flight battery	4S 6000 mA·h 35C LiPo
RC Servos	Henge MD933 servos
Airspeed sensor	4525DO Modul airspeed sensor
GPS with compass module	uBlox LEA-6H GPS with HMC5883L digital compass
Radio range	1 km*
Flight time	40 min*
Area coverage	100 ha*
Minimum speed	9.8 m/s

* Specifications reflect estimated values at ideal operating conditions. Environmental conditions can affect flight time and area coverage.

Table 7. Position and ID of individual trees

Tree ID	Latitude	Longitude
1	103.25269	-1.951613
2	103.24322	-1.950781
3	103.24700	-1.946587
4	103.26290	-1.948260
5	103.24577	-1.945642
6	103.23861	-1.957845
7	103.24061	-1.949962
8	103.24430	-1.955150
9	103.23889	-1.956107
10	103.24809	-1.942348
11	103.24488	-1.948242
12	103.24534	-1.948009
13	103.24562	-1.947847
14	103.24599	-1.947684
15	103.24621	-1.947394
16	103.25906	-1.949920
17	103.24876	-1.956331
18	103.25823	-1.947262
19	103.25039	-1.947392

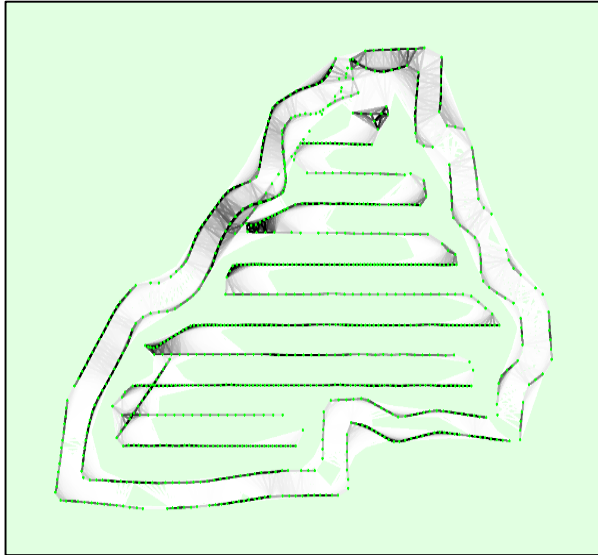


Figure 36. Display of the keypoint matches. It is showing a top view of the image computed positions with links between matching images. The color of the links indicates the number of matched 2D keypoints between the images. Darker color is indicating strong links and bright color is indicating weak links

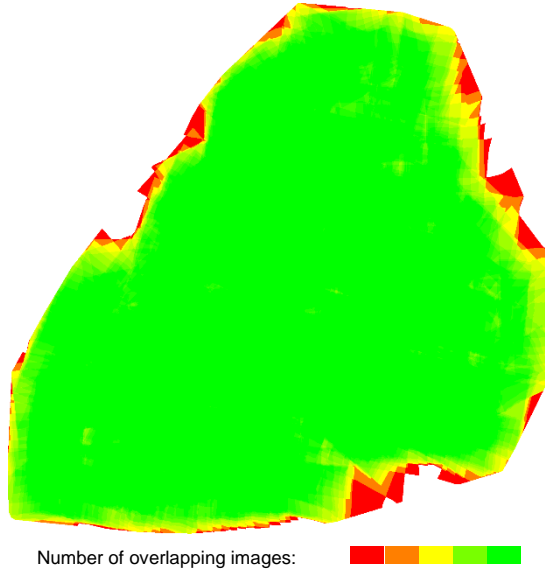


Figure 37. Representation of the number of overlapping images computed for each pixel of the orthomosaic. Red and yellow areas indicate low overlap for which poor results may be generated. Green areas indicate an overlap of over five images for every pixel

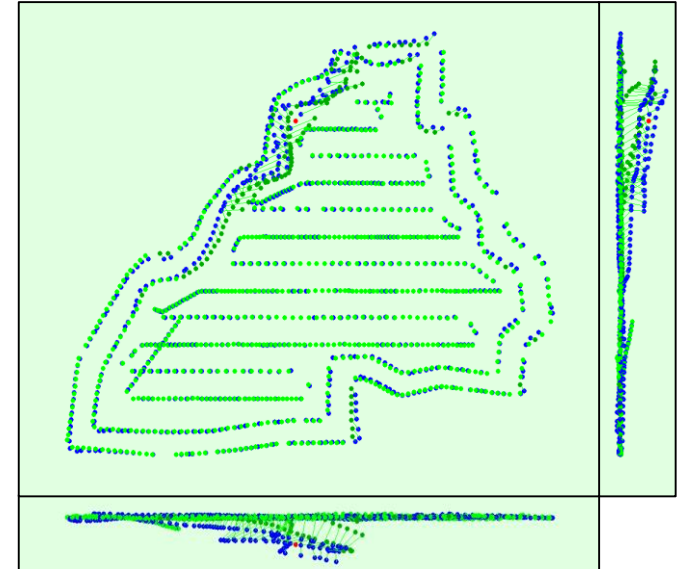


Figure 38. The offset between the initial (blue dots) and computed (green dots) image positions in the top-view (XY plane), front-view (XZ plane), and side-view (YZ plane). The red dot indicates the non-calibrated image

Table 8. Excluded altitudes from certain experimental tree island, due to incorrect GPS measurements.

Plot N°	Altitude from GPS (m)	Altitude from photogrammetry (m)
3	47.606987	40.50778
5	6.763002	54.21718
9	4.502375	50.67109
10	59.164062	57.19758
12	57.724091	53.01415
15	70.148621	64.82374
16	0.580854	54.11109
19	53.588722	48.205
21	5.572036	64.64605
22	44.250057	44.18436
24	58.310097	53.57635
26	4.645462	44.70439
29	56.804585	47.80345
32	52.464527	52.4588
34	52.225445	44.6961
35	49.826218	44.40873
38	44.356728	38.85632
40	2.047888	52.59072
46	58.367916	47.15128
49	70.893433	42.97958

Acknowledgements

Hereby, I would like to thank Prof. Dr. Dirk Hölscher and Prof. Dr. Holger Kreft from the Georg-August-University of Göttingen, who made this thesis possible for me and who have supported me with their supervision during the whole working process.

Furthermore, I also thank my counterparts Dr. Bambang Irawan from the University of Jambi and Dr. Leti Sundawat from the Bogor Agricultural University.

Very special thanks to Simon Wunderlin and Graham Usher from Conservation Drones. They were a great support to me and I do not know if I would have succeeded without their efforts.

I also thank Arite Hildebrandt for her huge help during the writing and for proofreading my draft.

Furthermore, I would like to thank Zulfi Kamal and Anne Gérard.

Statutory declaration

I hereby confirm that I composed my thesis independently without having used any other sources or means than stated therein.

Date: _____ Signature: _____